

MDPI

Review

Recent Progress of Self-Powered Optoelectronic Devices Based on 2D Materials

Jiyuan Xu¹, Zailan Zhang^{2,*}, Wei Zhang^{3,*} and Zhesheng Chen^{1,*}

- School of Material Science and Engineering, Nanjing University of Science and Technology, Nanjing 210094, China; jiyuanxu@njust.edu.cn
- School of Physics, Nanjing University of Science and Technology, Nanjing 210094, China
- Institute for Frontier Science, Nanjing University of Aeronautics and Astronautics, Nanjing 210016, China
- * Correspondence: zhangzailan@njust.edu.cn (Z.Z.); wei.zhang@nuaa.edu.cn (W.Z.); zhesheng.chen@njust.edu.cn (Z.C.)

Abstract: Harvesting energy through light radiation is an attractive solution for powering wireless devices in the future. In particular, self-driven optoelectronic devices are especially attractive for low-energy devices on the Internet of Things. Two-dimensional (2D) materials at atomic scale thicknesses are very attractive for future self-powered optoelectronic devices due to not only their unique electronic and optical properties, but also the feasibility to fabricate desirable heterostructures, which differ from their bulk counterparts and conventional optoelectronic materials. In this review, we mainly summarized the mechanism and performance of self-powered optoelectronic devices based on 2D materials. The figure of merit and mechanism of self-driving optoelectronic devices including the interface-junction effect, bulk photovoltaic effect, and photothermoelectric effect are discussed in detail. In addition, the recent progress on the performance of self-powered optoelectronic devices based on 2D materials is compared, followed by the perspective of this field. This review is aimed to give a generalized knowledge of 2D self-powered optoelectronic devices, and thus prompt the exploration and development of novel functional devices based on 2D materials.

Keywords: optoelectronic device; self-powered; 2D materials



Citation: Xu, J.; Zhang, Z.; Zhang, W.; Chen, Z. Recent Progress of Self-Powered Optoelectronic Devices Based on 2D Materials. *Processes* **2024**, *12*, 1728. https://doi.org/10.3390/ pr12081728

Academic Editor: Fang-Chung Chen

Received: 13 July 2024 Revised: 11 August 2024 Accepted: 14 August 2024 Published: 16 August 2024



Copyright: © 2024 by the authors. Licensee MDPI, Basel, Switzerland. This article is an open access article distributed under the terms and conditions of the Creative Commons Attribution (CC BY) license (https://creativecommons.org/licenses/by/4.0/).

1. Introduction

The Internet of Things (IoT) is a representative technical achievement of the fourth industrial revolution. Combined with radio frequency identification technology and cloud supercomputing technology, it ultimately realizes the direct information interaction between things and people. In the face of today's vast scale of IoT devices, sustainable energy supply has become a more challenging problem [1,2]. From the perspective of sustainable development, it is essential to make full use of the environmental characteristics of IoT devices and to develop new types of energy materials that can absorb environmental energy to continuously supply electricity [3–5]. In the last decades, many bulk semiconductors and their heterostructures have been reported for self–powered optoelectronic devices, such as ZnO [6,7], TiO₂ [8], SnO₂ [9], and so on. However, the drawbacks of the devices based on these materials include less flexibility and tunability, which limit further applications in the field of self–powered optoelectronic devices.

Compared with conventional bulk materials [10,11], two–dimensional (2D) materials have shown many advantages in the field of self–powered optoelectronic devices in recent years [12–14]. The concept of 2D materials was first introduced in 2004 when single layer graphene was successfully isolated from bulk graphite through mechanical exfoliation [15]. Nowadays, various other 2D layered nanomaterials akin to graphene have been investigated including monolithic 2D materials such as black phosphorus (BP) [16,17], hexagonal boron nitride (h–BN) [18,19], and transition metal chalcogenides (TMDs) [20–26]. This diverse array of 2D materials offers extensive options for material selection ranging from

Processes 2024, 12, 1728 2 of 27

zero-bandgap metals to large-bandgap insulators with tunable bandgaps spanning from infrared to ultraviolet wavelengths. Due to the quantum size effect, the electronic band structures of 2D materials are very different from their parent compounds, which can lead to an indirect-to-direct bandgap transition as a function of thickness [27]. In this case, the light absorption capability of two-dimensional layered materials may surpass that of bulk materials [28]. Additionally, layers of 2D materials can be stacked together to form heterostructures without considering lattice mismatch between the layers [29–38]. Therefore, the built-in potential at the interface can become significantly large by stacking desirable materials, which is a key parameter in realizing self-powered optoelectronic devices based on 2D heterostructures.

Significant efforts have been devoted to the exploration and realization of applications for two-dimensional materials in photovoltaic conversion and photodetection [39–46]. Here, we summarize the recent progress on self-powered optoelectronic devices based on 2D materials over the past few years. In this review, we first briefly introduce several key parameters used to determine device performance in the field of optoelectronic devices. Then, we discuss in detail the three main photoelectric conversion mechanisms of self-driven optoelectronic devices, which include the interface-junction effect, the bulk photovoltaic effect, and the photothermoelectric effect. The correlations between these effects are that the interface-junction effect primarily arises from the band alignment between the two adjacent materials, whereas the other two effects stem from the intrinsic properties of the individual 2D materials. In addition, the performance of self-powered optoelectronic devices based on these mechanisms is compared afterward. Finally, we discuss the challenges of self-powered optoelectronic devices and provide perspectives based on 2D materials. Figure 1 summarizes the self-powered optoelectronic devices based on 2D materials in this review. This review of recent advances and perspectives on 2D optoelectronic devices offers new insights into the exploration of new physical properties and aids in the design of novel devices with multi-functionalities and high performance based on 2D materials.

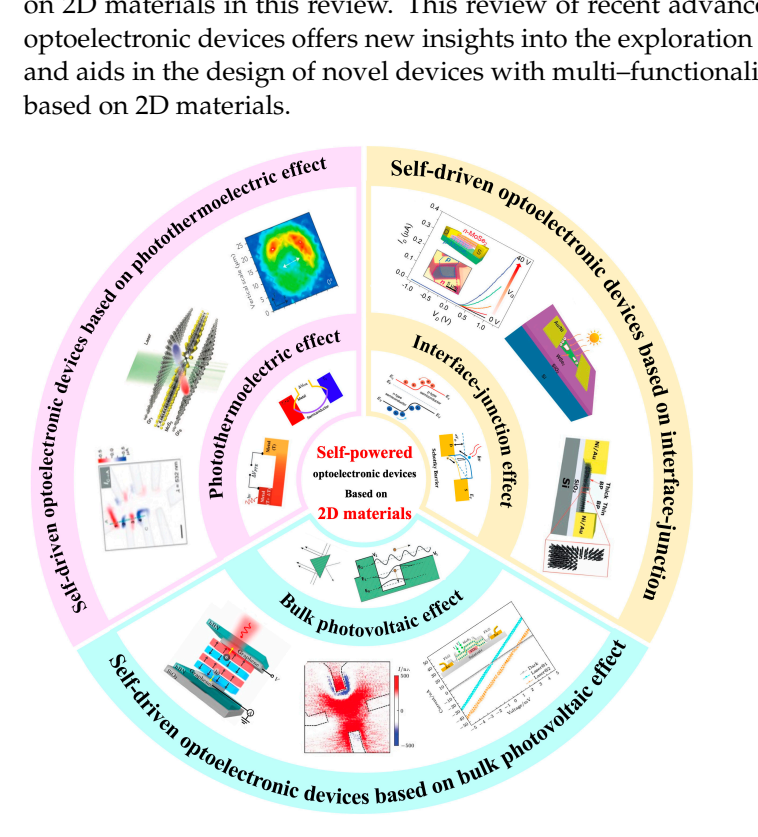


Figure 1. A brief summarization of self–powered optoelectronic devices based on 2D materials, with three mechanisms including the interface–junction effect, bulk photovoltaic effect, and photothermoelectric effect. (Reproduced with permission from [40,47–58]. Copyright 2015, 2017, 2018, Wiley–VCH; Copyright 2015, Royal Society of Chemistry; Copyright 2021, AAAS. Copyright 2015, 2016, 2021, Springer Nature; Copyright 2009, American Chemical Society).

Processes 2024, 12, 1728 3 of 27

2. Figures of Merit in Optoelectronic Devices

The key figures of merit used to characterize the performance of optoelectronic devices include the switching ratio, responsivity, response time, open—circuit voltage, short—circuit current, fill factor, photovoltaic conversion efficiency, and external quantum efficiency. The definitions of these parameters are listed below.

Optical switching ratio (r): r is defined as the ratio of the photocurrent to the dark current [59].

$$r = \frac{I_{ph}}{I_{dark}} = \frac{I_{light} - I_{dark}}{I_{dark}} \tag{1}$$

where I_{ph} is the photocurrent, I_{dark} represents the dark current, and I_{light} represents the current value under light. By suppressing the dark current and increasing the light current, the optical switching ratio of a photodetector can be significantly improved.

Responsivity (*R*): *R* measures the sensitivity of the detector's response to an incident light signal [60]. When light with power *P* is incident on the detector, the photogenerated current or photogenerated voltage output from the detector is expressed as follows:

$$R = I_p / P \tag{2}$$

 I_p represents the photogenerated current, and P is referred to as the power of the unit area.

Response time: The response time is a parameter that reacts to the response speed of the photodetector. Generally, the time used to increase the photocurrent from 10% of the maximum value to 90% is defined as the rise time, and from 90% down to 10% is defined as the fall time. The smaller these times are, the faster the photodetector responds to changes in light [47].

Open–circuit voltage (V_{oc}): V_{oc} is the maximum voltage of the photovoltaic device generated at a current of zero. The theoretical equation for the open–circuit voltage can be expressed as below [61].

$$V_{oc} = \frac{k_B T}{q} \ln(\frac{J_{sc}}{J_0} + 1) \tag{3}$$

where k_B is the Boltzmann constant, T is the absolute temperature, q is the charge, J_{sc} is the short–circuit current density, and J_0 is the reverse saturation current density. The open–circuit voltage can be affected by the energy levels of the materials, the work function of the electrode material, and the charge–carrier complex rate.

Short–circuit current density (J_{sc}): J_{sc} is the photogenerated current density when no bias voltage is applied, in which the built–in electric field drives the charge carriers to move in the circuit. Considering the actual and potential losses in a photovoltaic device, the short–circuit current density is given by the following equation [62].

$$J_{sc} = J_{ph} - J_0 \left[exp \left(\frac{eV + eJR_s}{nk_BT} \right) - 1 \right] - \frac{V + JR_s}{R_{sh}}$$

$$\tag{4}$$

where J_{ph} the photogenerated current density, n is the diode ideal coefficient, R_s is the equivalent series resistance, and R_{sh} is the equivalent parallel resistance. The short–circuit current density is related to the absorption properties of the photoactive layer, the charge carrier generation rate, transport rate, and extraction rate.

Filling factor (*FF*): *FF* is the ratio of the actual maximum output power density to the product of the open–circuit voltage and short–circuit current density [63].

$$FF = \frac{P_{Max}}{V_{oc}J_{sc}} = \frac{V_{MP}J_{MP}}{V_{oc}J_{sc}}$$
 (5)

Processes 2024, 12, 1728 4 of 27

Photoelectric conversion efficiency (*PCE*): *PCE* measures the effectiveness of a device in converting incident light energy into electrical energy. The formula of *PCE* can be expressed as follows [64].

 $PCE = \frac{P_{Max}}{P_{in}} = \frac{V_{oc}J_{sc}FF}{P_{in}}$ (6)

where P_{in} is the optical power density of incident light.

External quantum efficiency (*EQE*): *EQE* is defined as the ratio of the number of charge carriers (electrons or holes) collected by the device to the number of incident photons. Essentially, *EQE* measures how efficiently a device converts incoming photons into electrical current [65]. *EQE* is expressed as follows:

$$EQE = \frac{n_e}{n_{total\ photon}} = \frac{R(hc)}{(e\lambda)}$$
 (7)

High *EQE* values indicate that the device is highly efficient at converting light into electrical energy, which is crucial for applications such as solar cells, photodetectors, and other light–sensitive devices.

Internal quantum efficiency (*IQE*): *IQE* is commonly defined as the ratio of the number of electron–hole pairs or carriers generated within a device to the number of photons it absorbs. *IQE* is essentially a measure of the efficiency with which absorbed photons are converted to electron–hole pairs within the device compared to the total number of photons absorbed [66].

3. Mechanisms of Self-Powered Optoelectronic Devices

Self–powered optoelectronic devices can operate without an external power source by harnessing various intrinsic effects to generate and separate charge carriers. In 2D materials, the main mechanisms of self–powered optoelectronic devices can be divided into three types: interface–junction effect, bulk photovoltaic effect, and photothermoelectric effect. The details on the three mechanisms are discussed in detail in the following.

3.1. Interface-Junction Effect

The interface–junction effect occurs at the boundary of two different materials, such as in p–n junctions, Schottky junctions, or heterojunctions. When light is absorbed at the interface, electron–hole pairs are generated. The built–in electric field at the junction separates these charge carriers, directing electrons towards one material and holes towards another, thereby generating a photocurrent. According to the photocurrent generation mechanism, the interface–junction effect can be divided into two categories: p–n junctions and Schottky junctions, as shown in Figure 2a,b, because these two effects both have built–in electric fields that can accelerate the separation of photogenerated electron–hole pairs [35,48,67].

3.1.1. P-N Junction

As an important part of semiconductor devices, p–n junctions have a good application potential in the field of self–powered photodetectors. When a p–type semiconductor and an n–type semiconductor are stacked together, due to the carrier concentration gradient in the junction, the carriers diffuse into the region of lower concentration carriers and form a space charge layer on both sides of the interface. The p–region of the p–n junction is a negative charge region, and the n–region is a positive charge region, which results in the formation of a strong localized electric field from the n–region to the p–region at the junction. When the p–n junction is illuminated, the photogenerated electrons and holes will move in a direction under the localized electric field of the junction, thus generating photocurrents. In recent years, many studies of p–n junction self–powered optoelectronic devices based on two–dimensional materials have been reported. According to their structural characteristics, p–n junctions based on 2D materials can be divided into 2D lateral heterojunctions [68–70],

Processes 2024, 12, 1728 5 of 27

2D vertical heterojunctions [30,71,72], and hybrid dimensional heterojunctions based on 2D materials (for example, growing nanowires or depositing nanoparticles and quantum dots on 2D materials) [73–78].

The 2D lateral p-n heterostructure as a classic 2D/2D heterojunction discloses some new characteristics and provides a new template for building heterojunctions based on two-dimensional optoelectronic devices [79–81]. In general, lateral p-n heterojunctions can only be fabricated by local modifications (chemical and physical doping, surface etching) and direct growth methods because the 2D materials are jointly in-plane bonded. Therefore, the lateral 2D heterojunction can provide more closely contacting interfaces. In addition, due to the larger spatial spacing of 2D materials, lateral heterostructures are easily tuned for band offset. As shown in Figure 2c, other 2D materials are formed at the edges of the 2D materials, which are bonded together in the form of lateral heterojunctions. Xu et al. [82] successfully prepared a WSe₂-MoS₂ p-n junction using an epitaxial two-step growth method. The WSe₂-MoS₂ p-n junction exhibited a remarkable photovoltaic effect at zero bias, with a V_{oc} of about 0.22 V and an I_{sc} of about 7.7 pA (Figure 2d). This p-n heterojunction creates a significant built-in electric field at the contact interface, facilitating the separation of photogenerated electron-hole pairs without the need for an applied voltage. Recently, Wang et al. [49] experimentally demonstrated a gate-tunable BP lateral heterojunction diode for high-performance photovoltaic application (Figure 2e-g). Modulation of the thickness leads to bandgap variations and energy-band misalignment between BP flakes, obviating the necessity for a split–gate structure or selective chemical doping or transfer processes. By adjusting the V_g , the heterojunction device exhibits diode characteristics within a specific V_g range and can harvest energy in the visible and near-infrared spectral ranges. Specifically, at 660 nm, the device achieved a V_{oc} of about 210 mV and an I_{SC} about 1.5 nA at a power density of 3.6 W cm⁻², resulting in an external quantum efficiency of 7.4 percent, surpassing that of split-gated and chemically doped homojunctions.

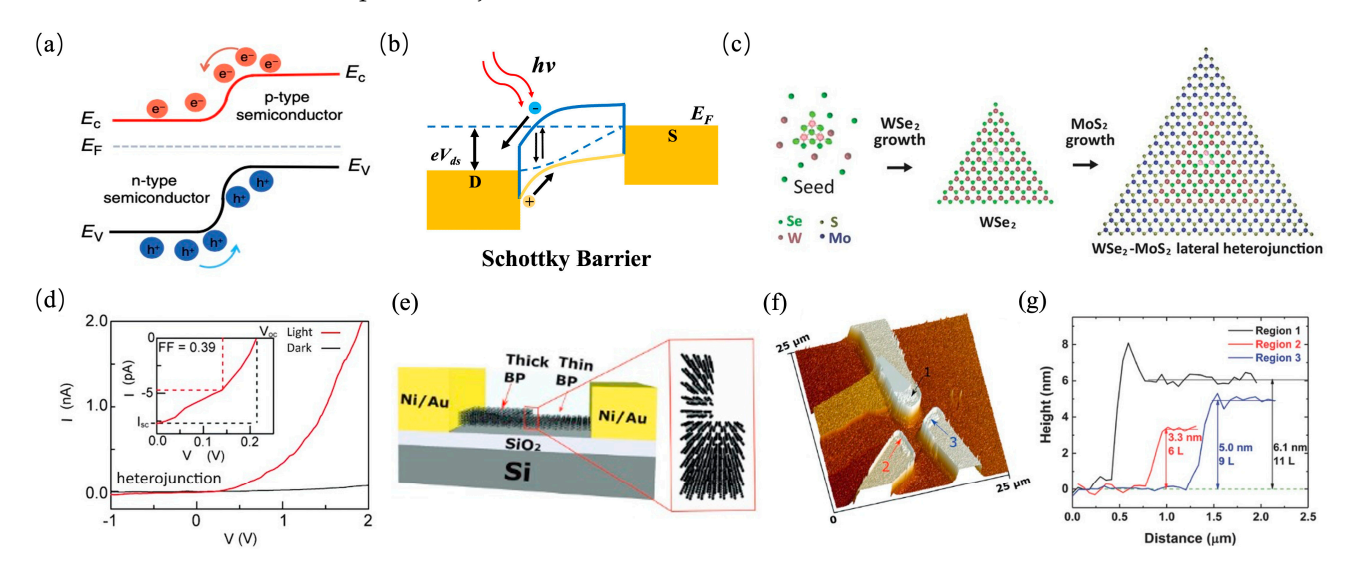


Figure 2. (a) Schematic diagram of the energy band structure of photodetectors based on the p-n junction. Reproduced with permission [48]. Copyright 2020, Springer Nature. (b) Schematic images of PVE originating from a metal-semiconductor Schottky barrier. Reproduced with permission [47]. Copyright 2018, Wiley-VCH. (c,d) Formation of a WSe₂-MoS₂ heterostructure and the electrical properties of the devices based on the heterojunction. Reproduced with permission [82]. Copyright 2015, AAAS. (e-g) Schematic illustration of the lateral black phosphorus heterojunction structure and 3D topography image from AFM tapping. Reproduced with permission [49]. Copyright 2017, Wiley-VCH.

The 2D materials can be separated from the bulk materials and stacked together to form a vertical heterojunction, creating a new structure that greatly expands the potential

Processes **2024**, 12, 1728 6 of 27

applications of 2D materials [83-85]. This artificial structure enables the production of artificial materials with exceptional properties not found in nature. The mechanical stacking method represents the simplest approach for constructing any two-dimensional vertical heterostructure. For example, Tu et al. [86] built a transistor based on the BP-MoS₂ vertical p-n heterojunction, as illustrated in Figure 3a. Figure 3b depicts a reflected image of the p-n junction between BP and MoS₂ flakes, with the edge of the electrodes indicated by grey dashed lines. The blue and purple dashed lines in these figures delineate the BP and MoS₂ crystals, respectively. Under zero gate bias, a p-n junction forms at the BP-MoS₂ interface, leading to efficient electron-hole pair separation. This separated pair generates a substantial photocurrent signal (Figure 3c). Furthermore, employing graphene as an electrode instead of metal electrodes can result in faster photoresponse times [87]. This result demonstrates that using graphene as an electrode can effectively address the contact issue between the metal electrode and semiconductor materials in the photodetector while enhancing their photoresponse performance. Subsequently, Zhong et al. [88] fabricated a high-performance self-powered photodetector based on a graphene interlayer PdSe₂/MoSe₂ vertical p-n heterojunction (Figure 3d). Due to the built-in electric field generated by the p-n junction, the photodetector displayed outstanding self-powered behavior independent of an external power source. Additionally, as can be seen in Figure 3e,f, its light response rate reaches up to 651 mA W^{-1} and the response speed is up to 41.7/62.5 μ s, surpassing most reported vertical p-n heterojunction photodetectors. Furthermore, Li et al. [89] built a MoS₂ vertical p–n homojunction based on a single flake (Figure 3g–i). Under forward bias voltages at V_G = 60 V and V_D = 1 V, the time–resolved features demonstrate a dependable photoresponse with a stabilized I_{on}/I_{off} of 100. Moreover, when the gate is grounded, the MoS₂ p-n junction functions as a solar cell with estimated energy conversion performance metrics including efficiency at 0.4%, fill factor at 0.22, and light responsiveness at 30 mA W^{-1} . In another study, Jin et al. [50] effectively synthesized p-type MoSe₂ (inherently n-type) flakes through doping with Nb elements and constructed an ideal MoSe₂ vertical p-n junction (Figure 3j,k). The device shows a high performance as a function of gate voltage.

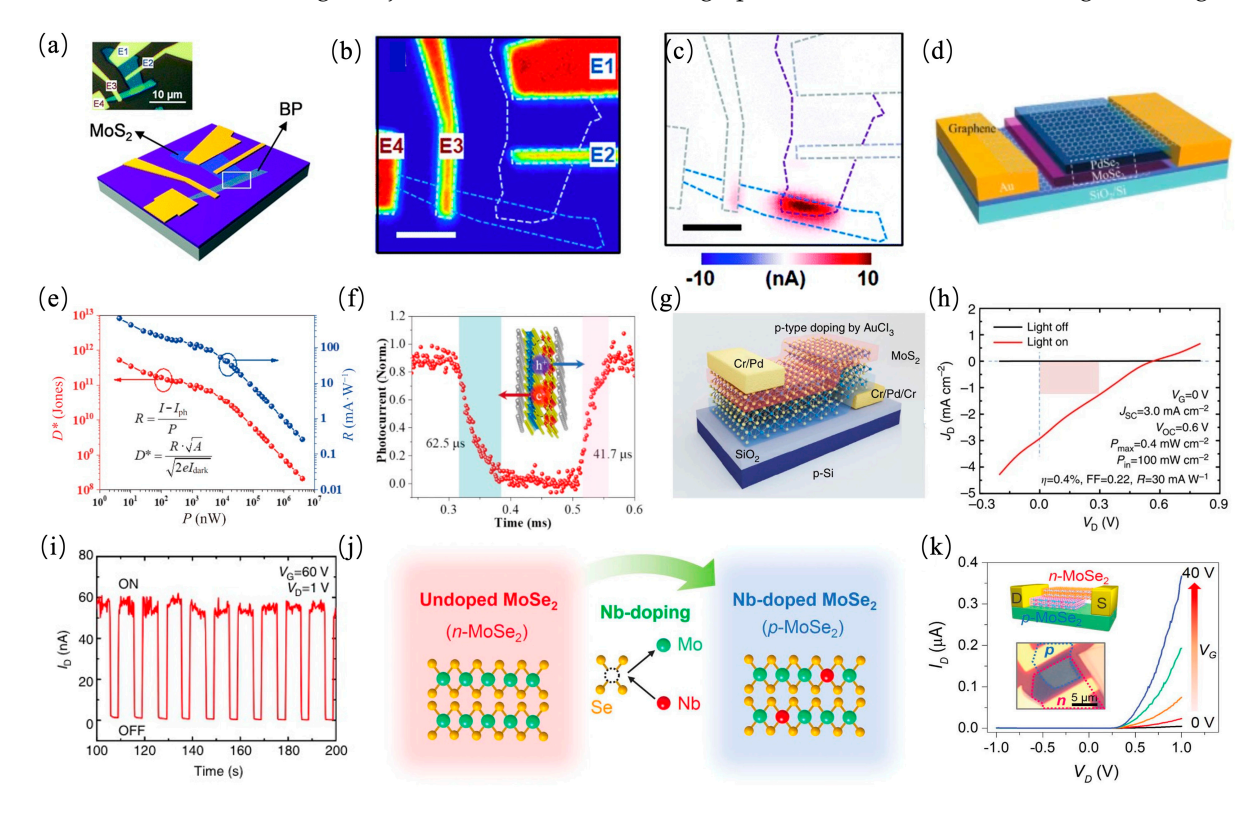


Figure 3. (a–c) Schematic illustration of a BP–MoS₂ p–n junction and photocurrent mapping at zero bias voltage. Reproduced with permission [86]. Copyright 2015. Royal Society of Chemistry.

Processes 2024, 12, 1728 7 of 27

(**d**–**f**) Schematic structure and performance of a vertically stacked graphene/MoSe₂/PdSe₂/graphene p–n heterojunction photodetector. Reproduced with permission [88]. Copyright 2021, Springer Nature. (**g**–**i**) Schematic diagram of vertical p–n homojunction of MoS₂ obtained by chemical doping and its optoelectronic performance. Reproduced with permission [89]. Copyright 2015, Springer Nature. (**j**–**k**) Schematics on Nb–doping mechanism for p–type MoSe₂ and the performance of the MoSe₂ homojunction device. Reproduced with permission [50]. Copyright 2015, Wiley–VCH.

In addition to the junctions consisting solely of layers of 2D materials, there are numerous mixed p-n junctions, similar to 2D-3D heterojunctions, 2D-1D heterojunctions, and 2D-0D heterojunctions. For illustration, Xie et al. [90] directly grew a multilayer PtSe2 film on a silicon substrate to form a 2D-3D PtSe₂/Si p-n heterojunction (Figure 4a-c). Due to the powerful built-in electric field at the p-n junction interface, the PtSe₂/Si p-n heterojunction displays a remarkable photovoltaic effect and can realize self-powered behavior at zero bias. The photodetectors operate in both photovoltage and photocurrent modes with responsivity values up to 5.26×10^6 V W⁻¹ and 520 mA W⁻¹ at 808 nm, respectively. The on/off ratio, specific detectivity, and response speed are 1.5×10^5 , 3.26×10^{13} Jones, and 55.3/170.5 µs, respectively. As shown in Figure 4d, Lin et al. [91] studied a 2D-0D graphene/CdTe heterostructure by covering a layer of ultrathin CdSe quantum dots on graphene which increased the power conversion efficiency from 2.08% to 3.10% (Figure 4e). In addition, Wang et al. [92] demonstrated a high performance optoelectronic device based on a 2D-0D graphene-perovskite heterostructure. As can be seen in Figure 4f-h, the responsivity is approximately 6.0×10^5 A W⁻¹ and the photoconductive gain is approximately 10⁹ electrons per photon. High-performance single CdS nanowire (NW) and nanobelt (NB) Schottky junction solar cells were reported by Ye et al. [93]. A typical as-fabricated NW solar cell exhibits excellent photovoltaic behavior with a V_{oc} of about 0.15 V and an I_{sc} of about 275.0 pA, and an energy conversion efficiency of up to ~1.65%, as shown in Figure 4i,j. Additionally, Tsai et al. [94] explored two planar nanostructures, graphene and CdSe nanobelts, for constructing Schottky junction solar cells with a V_{oc} of about 0.5 V and efficiencies in the order of 0.1% (Figure 4k,l).

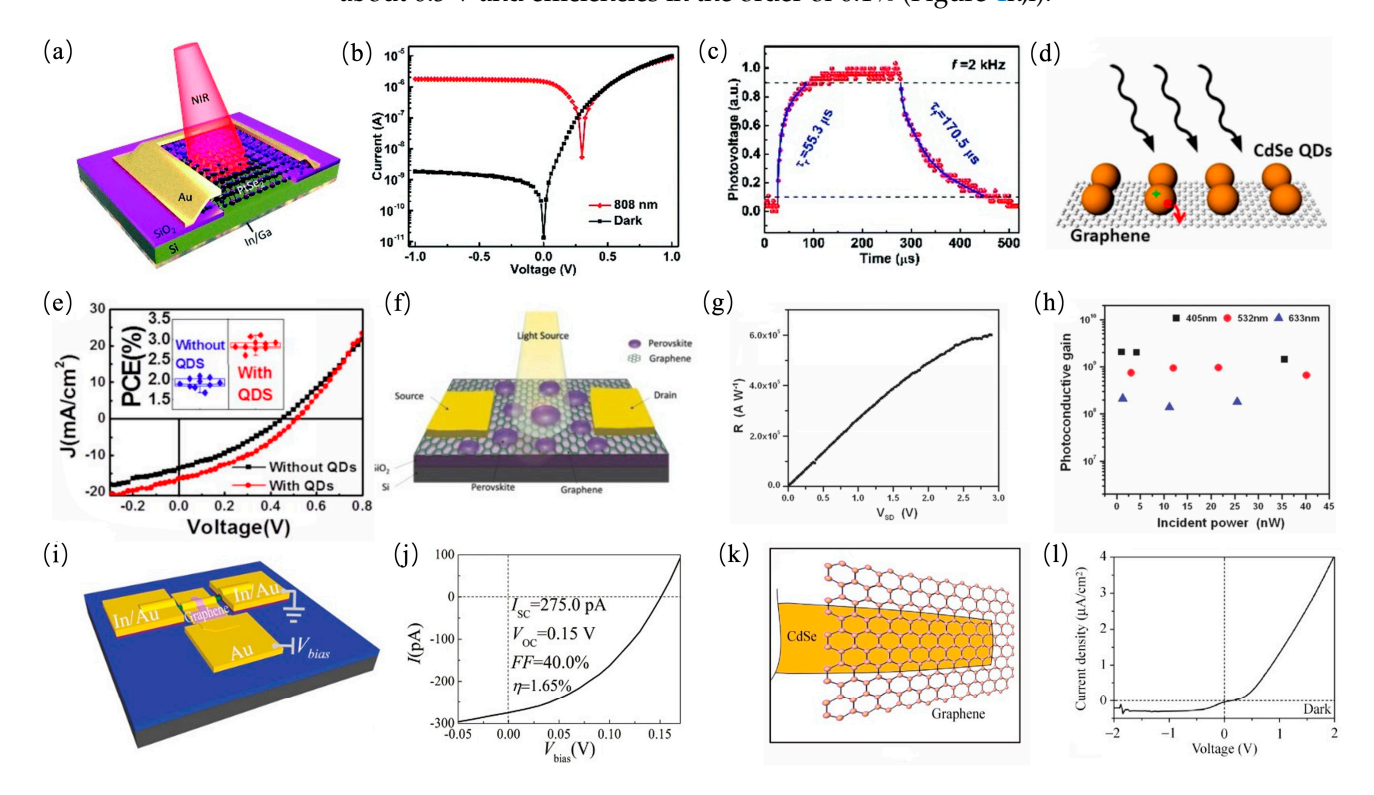


Figure 4. (a–c) Schematic of the PtSe₂/Si heterojunction photodetector and photodetection performance. Reproduced with permission [90]. Copyright 2018, Royal Society of Chemistry. (d,e) Schematic of the

Processes 2024. 12. 1728 8 of 27

graphene/CdTe heterojunction photodetector and solar cell performance. Reproduced with permission [91]. Copyright 2015, AIP Publishing. (f-h) Schematic configuration and photodetection performance of a graphene–perovskite phototransistor. Reproduced with permission [92]. Copyright 2015, Wiley–VCH. (i,j) Schematic configuration and solar cell performance of NW/graphene. Reproduced with permission [93]. Copyright 2010, American Chemical Society. (k,l) Schematic configuration and solar cell performance of CdSe/graphene. Reproduced with permission [94]. Copyright 2011, Springer Nature.

3.1.2. Schottky Junction

For previous photodetectors and solar cells, ohmic contact is usually established between two metal electrodes and a semiconductor material. Such optoelectronic devices depend on an external power supply to separate the photogenerated electron–hole pairs to achieve photoresponsive behavior [95–97]. However, an asymmetric Schottky contact device can be achieved if one of the two ohmic contact ends is replaced by a Schottky barrier contact. In contrast to ohmic contact devices, Schottky junction photodetectors exhibit high sensitivity and rapid response. Moreover, Schottky junction photodetectors leverage the built–in potential present at the nodes for the efficient separation and rapid transport of photogenerated carriers, enabling them to detect optical signals without requiring external voltage [46,98].

Schottky junctions may be formed at their interface, because of the various work functions and band arrangement between the 2D semiconductors and the metals. When the metal comes into contact with the semiconductor, electrons can migrate from the semiconductor to the metal, leading to the formation of a space charge region in the surface layer of the semiconductor that comprises positively charged impurity ions [99,100]. This results in an electric field directed from the semiconductor towards the metal. For instance, Fontana et al. [101] utilized hole-doped Pd and electron-doped Au as electrodes on multilayer MoS₂ to establish a Schottky junction at their interface. Under laser illumination, photoexcited electrons from Pd create electron-hole pairs in MoS₂ at the barrier and separate from the space charge at the interface due to the built-in potential. In Figure 5a,b, electrons accumulate on one side (Au) side while holes accumulate on another side (Pd), resulting in V_{oc} = 0.1 V. Additionally, Zhou et al. [51] fabricated a self–powered metal-semiconductor-metal (MSM) WSe2 photodetector with an asymmetric contact geometry Schottky contact by transferring the mechanically peeled WSe₂ flake onto the silicon substrate. In this study, a WSe₂ nanosheet with a special shape, such as a triangle or a slice with acute angles, was chosen for producing MSM photodetectors with asymmetric Schottky contacts, as shown in Figure 5c. This MSM Schottky junction photodetector exhibits a high responsivity of 2.31 A W⁻¹ under zero bias conditions and a V_{oc} of 0.42 V for MSM Schottky junction photodetectors featuring large differences in contact area (Figure 5d).

In addition, numerous studies have been conducted on Schottky junction self–powered photodetectors. Dai et al. [102] developed a highly sensitive and responsive self–powered device by depositing an array of gold plasma nanoparticles onto the surface of an InSe Schottky diode (Figure 5e–g). Furthermore, owing to the significant Schottky barrier difference between the active layer and the two asymmetric electrodes, the responsivity of the InSe/Au photodetector can reach 369 mA W⁻¹ and 244 mA W⁻¹ at the wavelength of 365 nm and 685 nm, under zero bias voltage conditions. Gong et al. [103] fabricated a vertical Schottky structure based on Au–MoS₂–ITO for use in a Schottky junction photodetector (Figure 5h–j). This device displays a rapid response time about 64 μ s, a stable photoresponsivity about 1 A W⁻¹, a high I_{on}/I_{off} ratio of 10⁶, and an ultralow dark current of 10⁻¹² A at zero bias voltage. Subsequently, a vertical Au–WSe₂–ITO Schottky junction photodetector was reported with substantially suppressed dark current to about 10⁻¹² A (Figure 5k,l) [104].

Processes 2024, 12, 1728 9 of 27

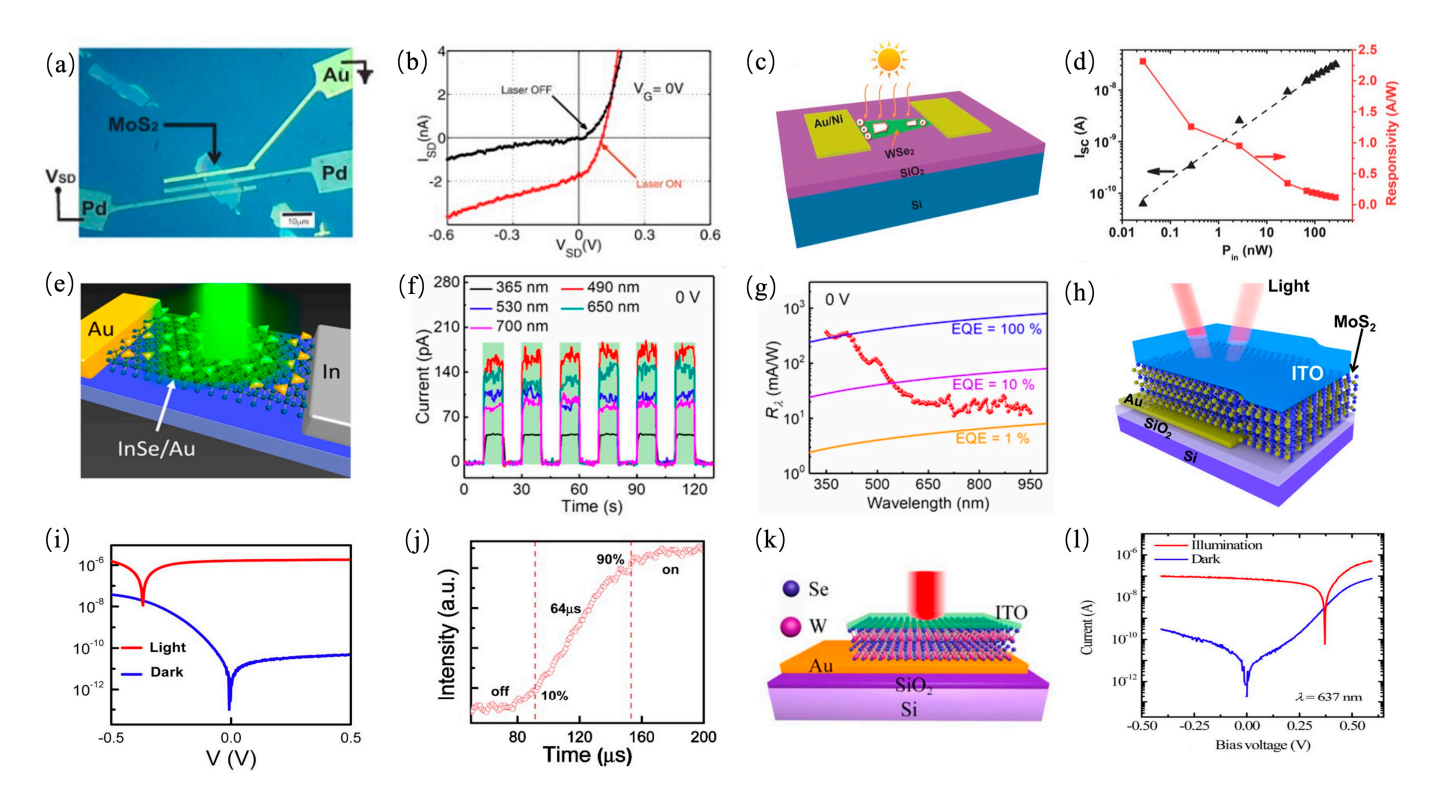


Figure 5. (**a**,**b**) Photovoltaic effect with Pd–Au bias configuration. Reproduced with permission [101]. Copyright 2013, Springer Nature. (**c**,**d**) 3D schematic device structure and photoelectric properties of metal–WSe₂–metal (MSM) photodetectors. Reproduced with permission [51]. Copyright 2018, Wiley–VCH. (**e**–**g**) Schematic diagram of the device structure of a pristine InSe self–powered photodetector and its photoelectric properties. Reproduced with permission [102]. Copyright 2018, American Chemical Society. (**h**–**j**) Schematic configuration and photodetector performance based on Au–MoS₂–ITO vertical Schottky junctions. Reproduced with permission [103]. Copyright 2017, IOP Publishing. (**k**,**l**) Schematic configuration and photodetector performance of a Au–WSe₂–ITO vertical Schottky junction. Reproduced with permission [104]. Copyright 2018, IOP Publishing.

Compared with p-n junction self-powered photodetectors, Schottky junction self-powered photodetectors offer numerous advantages, such as a simple structure, ease manufacture, low cost, and strong materials versatility. However, the early metal-semi-conductor Schottky photodetectors suffered from severely limited photoelectric conversion efficiency due to the strong light absorption characteristics of the thin metal layer. To address this issue, researchers have replaced the metal with ITO as the material for the light transmission layer. Nevertheless, ITO's brittleness, poor thermal stability, and difficulty in bending restrict its application as a transmittance layer in Schottky junction photodetectors. Graphene stands out as a typical 2D material with ultra-high transparency and good electron mobility, making it an ideal candidate for use as a transparent electrode with high optical transmittance and high conductivity.

Periyanagounder et al. [105] presented a self–powered photodetector based on a graphene/silicon Schottky junction (Figure 6a,b). The Schottky junction features a Schottky barrier of 0.76 eV, facilitating the efficient separation of photogenerated electron–hole pairs and enabling self–powered photoelectric detection behavior. The photodetector exhibits a responsiveness of 510 mA W $^{-1}$, an I_{on}/I_{off} ratio of 10^5 , and a photoresponse time of 130 µs at zero bias voltage. Luo et al. [106] constructed an photovoltaic device based on a graphene/single GaAs nanowire Schottky junction, which is shown in Figure 6c,d. When excited by a 532 nm laser, the device demonstrates a high photoresponsivity of 231 mA W $^{-1}$ and a rapid photoresponse/recovery time of 85/118 µs at zero bias. Under AM 1.5 G solar illumination, the device achieves a V_{oc} of 75.0 mV, an I_{sc} of 425 mA cm $^{-2}$, and a light conversion efficiency of 8.8%. The outstanding photovoltaic performance is

Processes 2024, 12, 1728 10 of 27

attributed to the strong built–in electric field with the Schottky junction, as well as the exceptional electron mobility and transparency properties exhibited by graphene. These findings underscore the efficacy of graphene–based Schottky junction photodetectors as efficient self–powered devices.

The performance of a graphene–based Schottky junction photodetector is determined by its Schottky barrier. Therefore, it is essential to identify an effective approach for adjusting the Schottky barrier of graphene–based Schottky junction photodetectors in order to enhance their light response. Xiang et al. [107] discovered that modifying the surface of MoO₃ film could significantly enhance the performance of a self–powered photodetector based on graphene/silicon Schottky junctions (Figure 6e). Yu et al. [108] improved the photoresponse performance of a self–powered photodetector based on a graphene/silicon Schottky junction by incorporating silicon quantum dots (Figure 6f,g). Under self–powered conditions, the responsivity was enhanced to 5.97 mA W $^{-1}$ and the corresponding detectivity reached 1.1×10^{11} cm Hz $^{0.5}$ W $^{-1}$. Additionally, Wu et al. [109] developed an effective method for enhancing the photoresponsive of graphene/GaAs Schottky junctions by introducing NaYF4:Yb3/Er3 upconversion nanoparticles (UCNPs) (Figure 6h,i).

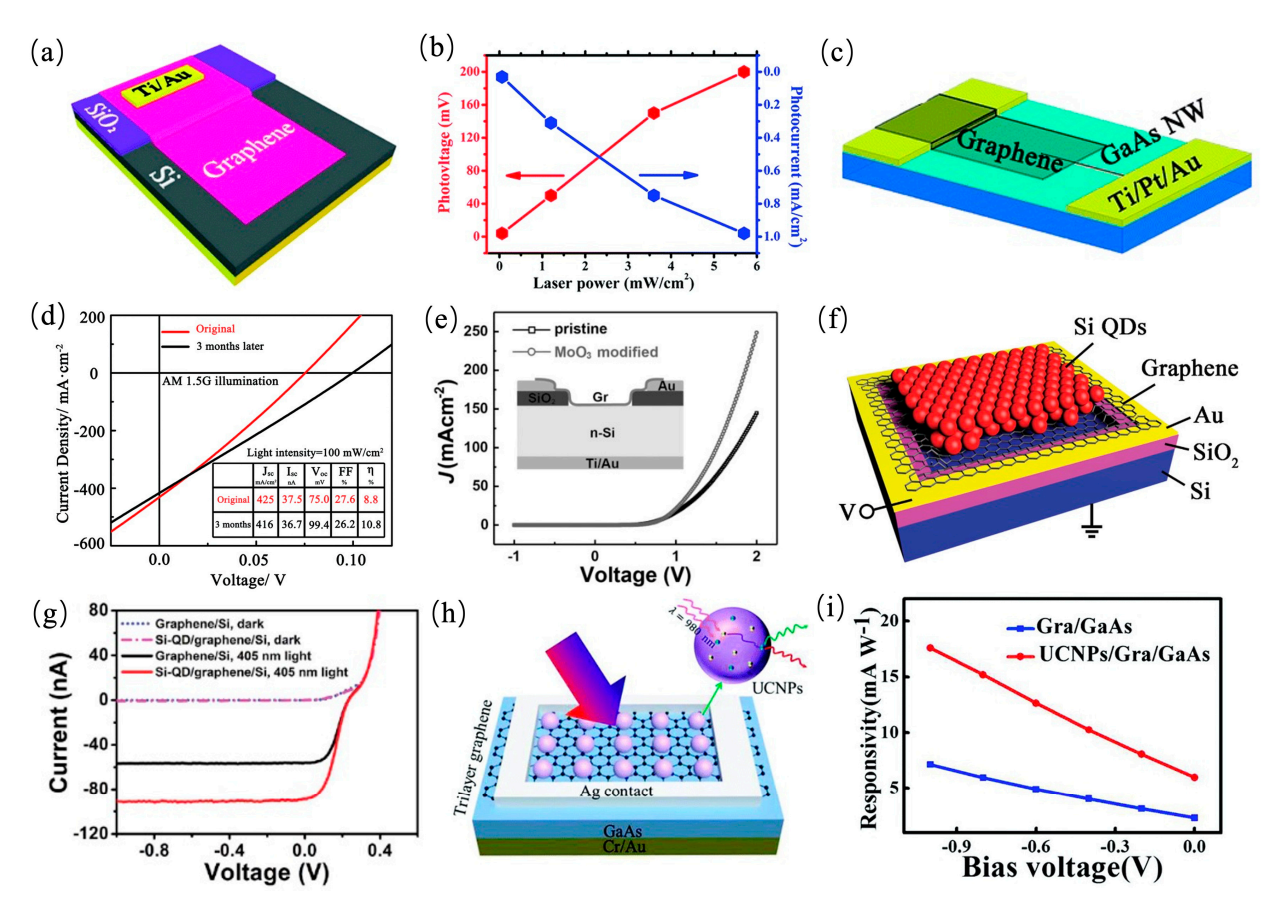


Figure 6. (**a**,**b**) Schematic diagram and photoelectric properties of graphene/silicon Schottky junction diode. Reproduced with permission [105]. Copyright 2018, Royal Society of Chemistry. (**c**,**d**) Schematic diagram and photovoltaic performance of a graphene/single GaAs nanowire Schottky junction. Reproduced with permission [106]. Copyright 2018, Royal Society of Chemistry. (**e**) J–V characteristics of a graphene/silicon Schottky junction device before and after 8 nm MoO₃ coating in dark conditions. Inset is the schematic illustration of the as–fabricated graphene/silicon device. Reproduced with permission [107]. Copyright 2015, Wiley–VCH. (**f**,**g**) Schematic diagram and photoelectric device performance of Si–QD/graphene/Si. Reproduced with permission [108]. Copyright 2016, Wiley–VCH. (**h**,**i**) Schematic diagram and photodetector performance of UCNPs/graphene/GaAs. Reproduced with permission [109]. Copyright 2018, Royal Society of Chemistry.

Processes 2024, 12, 1728 11 of 27

3.2. Bulk Photovoltaic Effect (BPVE)

In contrast to the photoelectric conversion based on the interface–junction effect caused by p–n junctions or Schottky junctions, the bulk photovoltaic effect is attributed to the structural polarization of a special material with a built–in electric field, which facilitates the separation of photogenerated carriers. Several models have been proposed to elucidate the mechanism of the bulk photovoltaic effect. One of the models is shown in Figure 7a, showing the BPVE resulting from randomly distributed scattering centers in a ferroelectric materials [52]. In the absence of external electric field interference, these asymmetrical centers can scatter carriers in all directions. When aligned in a single direction, however, they cause carrier scattering and drift, leading to a net current. Nevertheless, it is generally believed that the photocurrent generated by this model is local and short–lived. Another model is based on net current generation due to the asymmetric diffusion of electrons and holes across an asymmetric electrostatic barrier, as shown in Figure 7b [52].

BPVE is a type of second–order nonlinear photovoltaic response, which describes the steady–state photocurrent phenomenon arising from the non–centrosymmetric structure of a material under uniform illumination in the absence of an external electric field [110–112]. In contrast to traditional photovoltaic devices that rely on the internal electric field formed by the p–n junction for charge separation, BPVE achieves charge separation through spontaneous polarization generated by its non–centrosymmetric structure [113]. BPVE is distinguished by the following unique advantages: (1) The p–n junction structure is not required, and the device fabrication process avoids complex interface engineering and manufacturing processes. (2) The photocurrent and photovoltage generated by BPVE align with the spontaneous polarization of the material, and the open–circuit voltage is directly proportional to the thickness of the single crystal material, exceeding the bandgap (in contrast to traditional photovoltaic devices where the open–circuit voltage is lower than the bandgap). (3) BPVE exhibits considerable advantages in terms of the power conversion efficiency, material defect tolerance, and response speed [114,115].

This section summarizes the experimental progress in the study of the bulk photovoltaic effect in 2D materials. These materials can be classified according to the method of generating or modulating the bulk photovoltaic effect, as follows: (1) Single–component materials including 1D WS $_2$ nanotubes and 2D ferroelectric materials such as CuInP $_2$ S $_6$. (2) Two–dimensional materials stacking engineering involves the construction of non–centrosymmetric structures using 2D materials to generate spontaneous polarization. Two–dimensional materials stacking engineering uses 2D materials to build non–centrosymmetric structures to generate spontaneous polarization such as WSe $_2$ /BP heterojunctions. (3) 2D materials that generate or modulate BPVE through external forces, such as a magnetic field, stress, and so forth. Examples of such materials include CrI $_3$ and MoS $_2$.

Low–dimensional narrow–bandgap semiconductor materials are considered an effective approach to enhance the performance of BPVE. TMDs serve as a typical example of 2D semiconductors with a narrow bandgap. When the bulk material of TMDs is thinned to a monolayer, the block space inversion symmetry is broken. In 2019, Zhang et al. [116] observed BPVE in one–dimensional WS $_2$ nanotubes, exhibiting a photocurrent density several orders of magnitude higher than that of other materials documented in the literature. The monolayer WS $_2$ has a non–centrosymmetric and non–polar structure, which precludes the generation of significant BPVE photocurrents (Figure 7c). In contrast, the WS $_2$ nanotube structure with curved surfaces or stresses that break in–plane triple rotational symmetry and mirror symmetry is non–centrosymmetric and polar, resulting in stronger BPVE photocurrents (Figure 7d). This work not only demonstrates the potential of low–dimensional TMDs materials for BPVE applications, but also confirms the importance of reducing the structural symmetry of the materials to improve the photovoltaic conversion efficiency.

Processes **2024**, 12, 1728 12 of 27

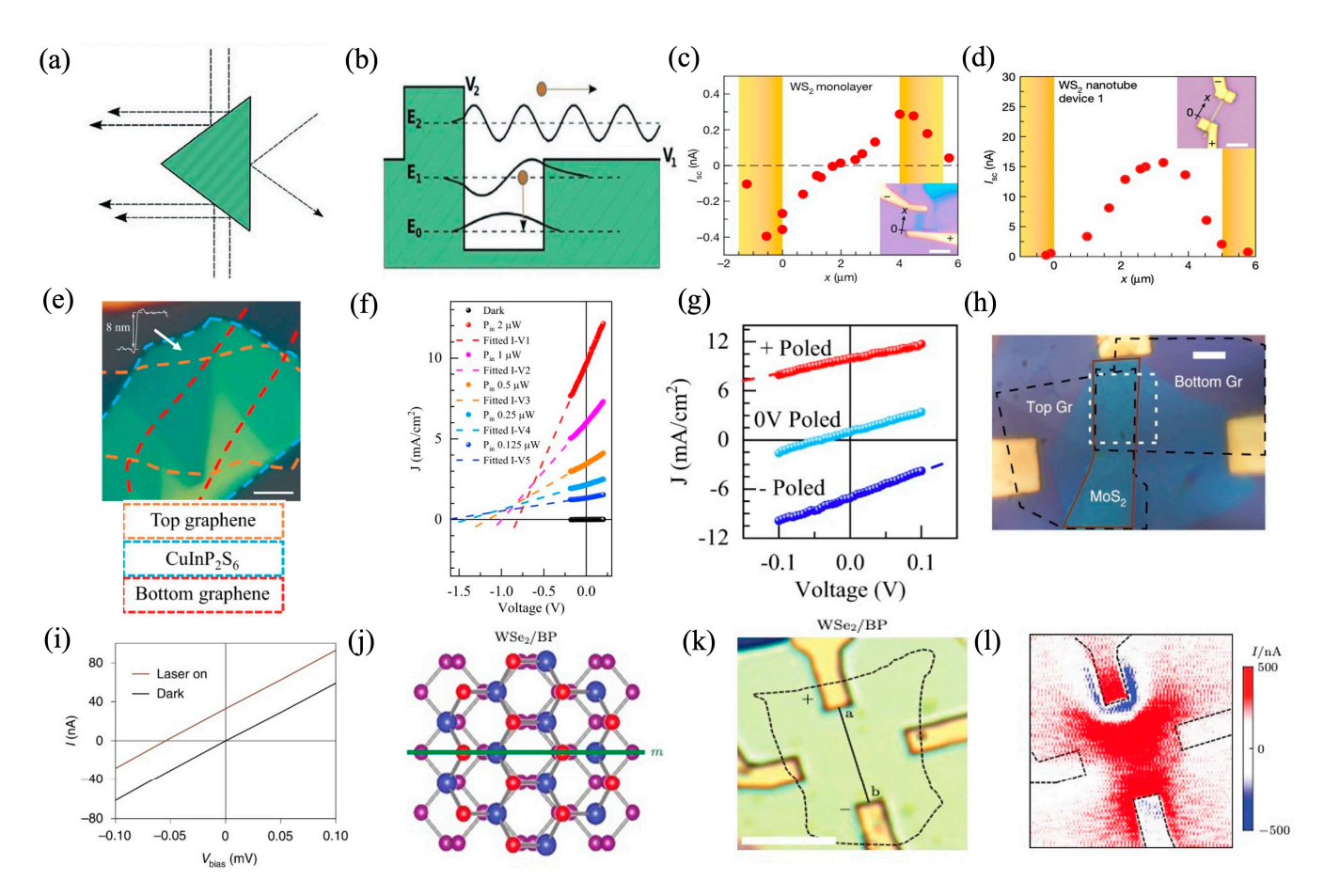


Figure 7. (**a,b**) Models for the bulk photovoltaic effect. Reproduced with permission [52]. Copyright 2015, Royal Society of Chemistry. (**c,d**) Bulk photovoltaic response of the WS₂ nanotube. Reproduced with permission [116]. Copyright 2019, Springer Nature. (**e-g**) Optical image and switchable photovoltaic effect in the graphene/CuInP₂S₆/graphene device. Reproduced with permission [117]. Copyright 2021, Springer Nature. (**h,i**) Optical image and photovoltaic performance of the graphene/3R–MoS₂/graphene heterostructure. Reproduced with permission [118]. Copyright 2022, Springer Nature. (**j-l**) Optical image and switchable photovoltaic effect in a WSe₂/BP heterointerface device. Reproduced with permission [53]. Copyright 2021, AAAS.

The ferroelectricity of 2D materials (GeS, SnTe, In₂Se₃, CuInP₂S₆, and 2D chalcogenides and their analogs, etc.) has been demonstrated theoretically and experimentally. Consequently, researchers have proposed utilizing 2D materials (e.g., CuInP₂S₆, α -In₂Se₃, and MoTe₂) to enhance the BPVE performance. In 2021, Li et al. [117] constructed the observation of the BPVE phenomenon in a 2D ultrathin ferroelectric material, CuInP₂S₆. The BPVE device in this work is a typical sandwich structure, comprising graphene/CuInP₂S₆/graphene as shown in Figure 7e. The 2D CuInP₂S₆ is a semiconductor with a bandgap of approximately 2.9 eV, while the ionic ferroelectric generates a bulk photovoltaic photocurrent. As illustrated in Figure 7f, the J-V output curves of the device under laser irradiation exhibit a linear increase in I_{sc} and V_{oc} with increasing laser irradiation intensity. At an irradiation intensity of 2 µW, an open-circuit voltage of $V_{oc} = -0.8 \text{ V}$ is generated, which is comparable to that of bulk ferroelectrics. Furthermore, the device photocurrent density J_{sc} of the ferroelectric material exhibits a notable increase following positive/negative voltage polarization. Additionally, the direction of the photocurrent reverses upon the reversal of the polarized electric field direction (Figure 7g), a phenomenon indicative of the ferroelectric photovoltaic effect.

The emergence of torsion electronics, exemplified by torsional graphene, has enabled the precise regulation of the electronic properties of 2D materials, opening new avenues in

Processes 2024, 12, 1728 13 of 27

fields such as superconductivity, Mott insulation, topological magnetism, and the quantum Hall effect. In 2022, Yang et al. [118] proposed a vertically stacked van der Waals (vdW) material based on a vertical stacking between two or more vdW materials. Figure 7h,i show an open–circuit voltage of $V_{oc} = -0.06\,\mathrm{V}$ in a graphene/3R–MoS₂/graphene heterostructure. This is a slip ferroelectric material. The discovery of 2D vdW stack–engineered ferroelectric materials has also led to the study of 2D vdW stack–engineered materials' BPVE.

In 2021, Akamatsu et al. [53] constructed a heterojunction interface of WSe₂ and BP with the objective of producing an in–plane spontaneous photovoltaic effect. The WSe₂/BP heterojunction breaks the spatial inversion symmetry, leading to a spontaneous photovoltaic effect, with the direction of the photocurrent aligned along the mirror direction (Figure 7j). The photocurrents were tested in three different devices, with no I_{sc} observed in the channel region of the single–layer WSe₂ and BP devices. In contrast, I_{sc} was clearly observed in the WSe₂/BP device, which suggests that the heterojunction structure leads to the generation of the spontaneous photovoltaic effect, as shown in Figure 7k,l. Furthermore, by comparing the photocurrent distributions at the two pairs of electrodes (along and perpendicular to the polarization direction), the researchers also investigated the relationship between the direction of photocurrent and the direction of spontaneous polarization in the WSe₂/BP device. Their findings demonstrated that the spontaneous polarization photocurrent originates from asymmetry–induced spontaneous polarization rather than from the Schottky barrier.

In addition to the intrinsic ferroelectricity of 2D vdW materials and the construction of 2D homo/heterojunctions to produce the bulk photovoltaic effect, researchers have also attempted to impose external constraints on 2D materials that are not intrinsically ferroelectric, with the aim of inducing or modulating the bulk photovoltaic effect. These external effects, including stress, temperature, magnetic field, interface engineering, and boundary conditions, result in the breakdown of the intrinsic symmetry. In 2019, Zhang et al. [119] proposed a theoretical switchable magneto photovoltaic effect in the 2D magnetic material chromium triiodide (CrI₃), as shown in Figure 8a. In 2021, Song et al. [54] conducted an experimental demonstration of the spin photovoltaic effect in the 2D magnetic material CrI₃. CrI₃ is a particularly intriguing layered antiferromagnetic material (AFM), with a single layer exhibiting out–of–plane ferromagnetism and antiferromagnetic mutual coupling between neighboring planes.

The I–V curve of this hBN/graphene/CrI₃/graphene/hBN heterojunction device shows that the four–layer CrI₃ produces a large spin photocurrent, as shown in Figure 8b. The four–layer CrI₃ was chosen for this work because, as the number of CrI₃ layers increases, multiple magnetic states become accessible, potentially enabling various states of the resulting spin photocurrent, which is defined as a photocurrent controlled by the spin degree of freedom [120]. Due to time–reversal symmetry breaking, the CrI₃ spin photocurrent is closely associated with the intensity of the magnetic field. The low and high photocurrent platforms generated by low and high magnetic fields correspond to the ground state and fully spin–polarized state of AFM, respectively (Figure 8c,d). It has been demonstrated that strain gradients can break the spatial inversion symmetry, which is a prerequisite for the generation of the bulk photovoltaic effect. Consequently, strain gradients can increase the pathway for the generation of the bulk photovoltaic effect. When a material with central symmetry is coupled with the flexoelectric effect, such a centrosymmetric material can produce the bulk photovoltaic effect, which can be referred as the flexoelectric effect [121].

In 2021, Jiang et al. [55] achieved the first flexural electro–photovoltaic effect in MoS₂. Figure 8e shows a MoS₂ wafer was positioned in part on a VO₂ micron belt (a phase–change material) and in part on a SiO₂ substrate (a non–phase–change material). The external conditions (e.g., temperature and electric field) control the structural phase transition of the phase–change material, which is expected to result in a uniform strain above the VO₂ microstrip and a strain gradient at the boundary between the SiO₂ substrate and the VO₂ microstrip. This leads to a non–zero dipole moment along the strain gradient, which is

Processes 2024. 12. 1728 14 of 27

known as a flexoelectric effect. As can be seen in Figure 8f, the MoS_2 flakes exhibit tensile strains in the surface region of the VO_2 micron band, with maximum strain gradients observed in the opposite direction in the regions on either side of the VO_2 micron band. As can be seen in Figure 8g, the short–circuit current in the region with a large strain gradient (Position 2, at the VO_2 boundary) is much higher than that in the region with a small strain gradient (Position 1, far away from the VO_2 boundary).

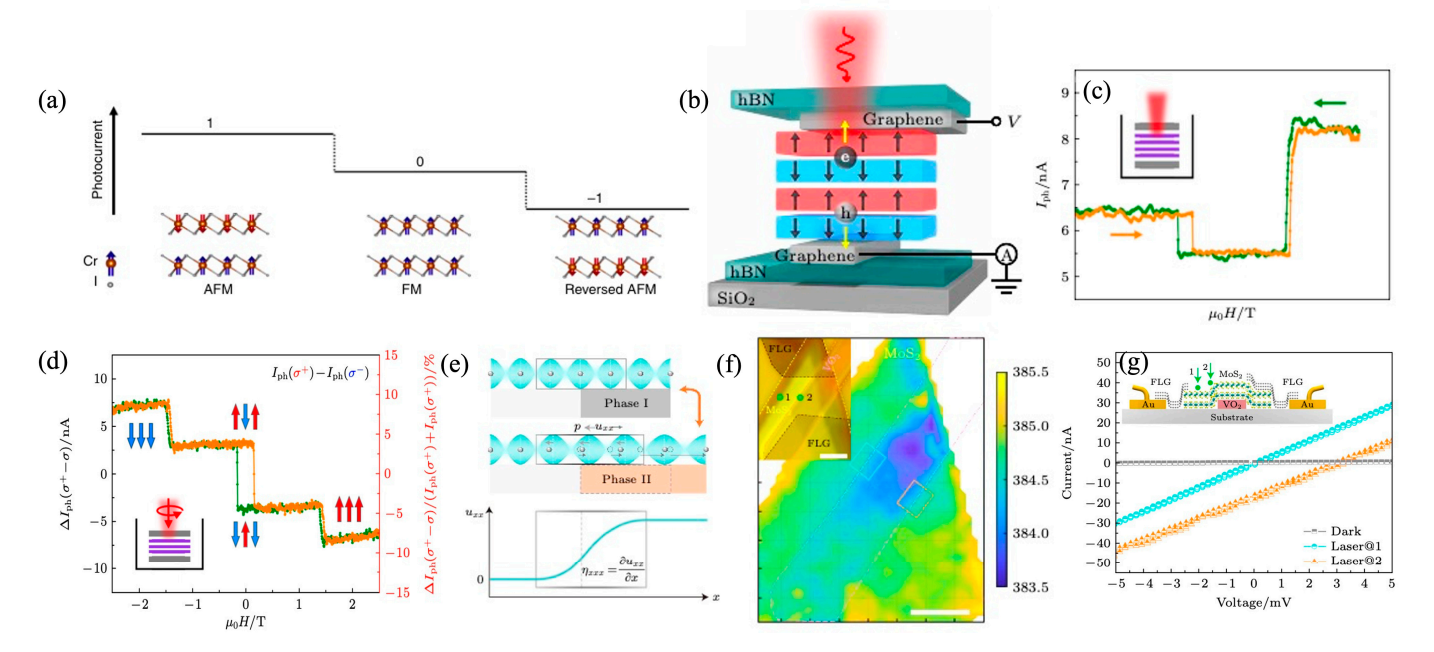


Figure 8. (a) The antiferromagnetic (AFM), ferromagnetic (FM), and reversed AFM phases display three distinct responses to a linearly polarized light—positive current state (1), zero current state (0), and negative current state (-1). Reproduced with permission [119]. Copyright 2019, Springer Nature. (b–d) Spin photovoltaic effect in a BN/graphene/CrI₃/Gr/BN junction device. Reproduced with permission [54]. Copyright 2021, AAAS. (e–g) Optical image and switchable photovoltaic effect in a MoS₂/VO₂ heterojunction device. Reproduced with permission [55]. Copyright 2021, Springer Nature.

3.3. Photothermoelectric Effect (PET)

The photothermoelectric effect is a phenomenon whereby light is unevenly distributed upon a material, thereby creating a temperature gradient and a potential difference within the material. As illustrated in Figure 9a, when light is incident upon a material, the radiant energy is transformed into the internal energy of the crystal lattice and electrons [122]. If the light distributed across the material is uneven, the material will heat up in a non–uniform manner, resulting in a temperature gradient (ΔT) within the material. The Seebeck effect describes how a temperature difference in a material can generate an electric potential difference based on both the temperature differential and the Seebeck coefficient of that particular material. In this instance, the material can direct charge carriers to move in a specific direction without external bias influence, thereby producing photocurrent [123,124].

The photothermoelectric effect is a photoelectric detection mechanism that leverages the thermal effect induced by light in combination with the thermoelectric properties of the material to generate an electrical signal. One notable advantage of this mechanism is its ability to operate at zero bias and at room temperature. The fundamental principle between the photothermoelectric effect lies in exploiting the variance in carrier chemical potential between the cold and hot ends of the material. Two particularly appealing characteristics of graphene photodetectors are their zero bandgap, enabling ultra–wideband light absorption, and high mobility, facilitating ultra–fast response speeds [15]. In theory, due to graphene's high thermal conductivity (suspended monolayer graphene about of $2500~\mathrm{W}~\mathrm{m}^{-1}~\mathrm{K}^{-1}$) and small Seebeck coefficient, it may not be an ideal thermoelectric

Processes 2024, 12, 1728 15 of 27

material [125,126]. Traditional photodetectors assume that electron temperature equals lattice temperature. However, non–equilibrium effects may arise in graphene under light excitation. As depicted in Figure 9b, an electron–hole pair is generated. Owing to strong electron–electron interaction, the charge carriers' absorption energy rapidly relaxes leading to charge carrier heating [123]. With weak electron–phonon interaction in graphene further inhibiting energy transfer from generated hot carriers to the lattice, thermoelectric effects can occur without involving phonon heat transport resulting in ultra–fast speeds and high response rates [127].

Xu et al. [128] conducted a detailed analysis for the first time on the origin of the photocurrent response at the interface of monolayer and bilayer graphene. In monolayer graphene (SLG), the energy–momentum dispersion relationship is linear, whereas in bilayer graphene (BLG), it is quadratic (Figure 9c). Consequently, as the Fermi level approaches the Dirac point, the density of states (DOS) of BLG exceeds that of SLG. When the carrier density is equal, the Fermi level of SLG surpasses that of BLG, leading to a higher built–in potential in SLG than in BLG upon contact between these two materials. Conversely, BLG exhibits a larger Seebeck coefficient due to its roughly proportional DOS. These characteristics result in opposite directions for photocurrents driven by the photovoltaic effect and the photothermal effect. Figure 9d depicts an image showing visible differences at different gate voltages and temperatures of 12 K at the interface between graphene and metal, as well as on single and double layers of graphene. Park et al. [56] studied that SLG is expected to display 2D features. The SLG device used in the study is shown in Figure 9e. Additionally, an SPCM image obtained from measuring a device using a 532 nm green laser is shown in Figure 9f.

The absence of a bandgap in graphene restricts its further application in digital electronics, where the high I_{on}/I_{off} ratio is crucial. TMDs with adjustable bandgaps are anticipated to address this limitation. For instance, bulk MoS₂ has an indirect bandgap of 1.2 eV, while monolayer MoS₂ has a direct bandgap of 1.8 eV [129]. Single–layer MoS₂ has been reported to exhibit a Seebeck coefficient of up to 30 mV K⁻¹ at room temperature due to its substantial bandgap [130]. Given the significant interband absorption, TMD–based photodetectors are expected to demonstrate an outstanding photothermal performance. Nevertheless, in most cases, the photovoltaic mechanism prevails owing to the large Schottky barrier at TMDs–metal junctions [131]. Therefore, reducing the height of the Schottky barrier is necessary for achieving a photothermal response in TMDs photodetectors.

Zhang et al. [132] observed that the generation and transport of photocurrent in multilayer MoS₂ are found to differ from those in other low-dimensional materials that only contribute with either a photovoltaic effect or photothermoelectric effect. In multilayer MoS₂, the PVE at the MoS₂-metal interface dominates in the accumulation regime whereas the hot-carrier-assisted PTE prevails in the depletion regime. In addition, the anomalously large Seebeck coefficient observed in multilayer MoS_2 , which has also been reported by others, is caused by hot photo-excited carriers that are not in thermal equilibrium with the MoS_2 lattice, as shown in Figure 11a–c. Buscema et al. [133] constructed a pronounced photothermoelectric response in a monolayer MoS₂ photodetector by establishing ohmic contact between MoS₂ and a low-work-function titanium electrode. The 2D spatial distribution of the photogenerated voltages excited by sub-bandgap and above-bandgap input is consistent, indicating the source of the photogenerated voltages in both cases (Figure 11d–f). The responsivities at the 532 and 750 nm wavelengths are 9.6 V W^{-1} and 1 V W^{−1}, respectively. Additionally, the back gate was utilized for adjusting the carrier density. As the system transitions from a low–resistance state ($\approx 1 \text{ M}\Omega$) to a high–resistance state $(>0.1~{\rm G}\Omega)$, the photothermoelectric voltage displays a significant two order of magnitude increase due to an elevated Seebeck coefficient estimated at $-3 \times 10^5 \,\mu V \, K^{-1}$. Clearly, the NEP value determined by the Johnson noise will be substantial in the high–resistance state, thereby constraining the practical applications of this large photothermoelectric voltage.

Processes 2024, 12, 1728 16 of 27

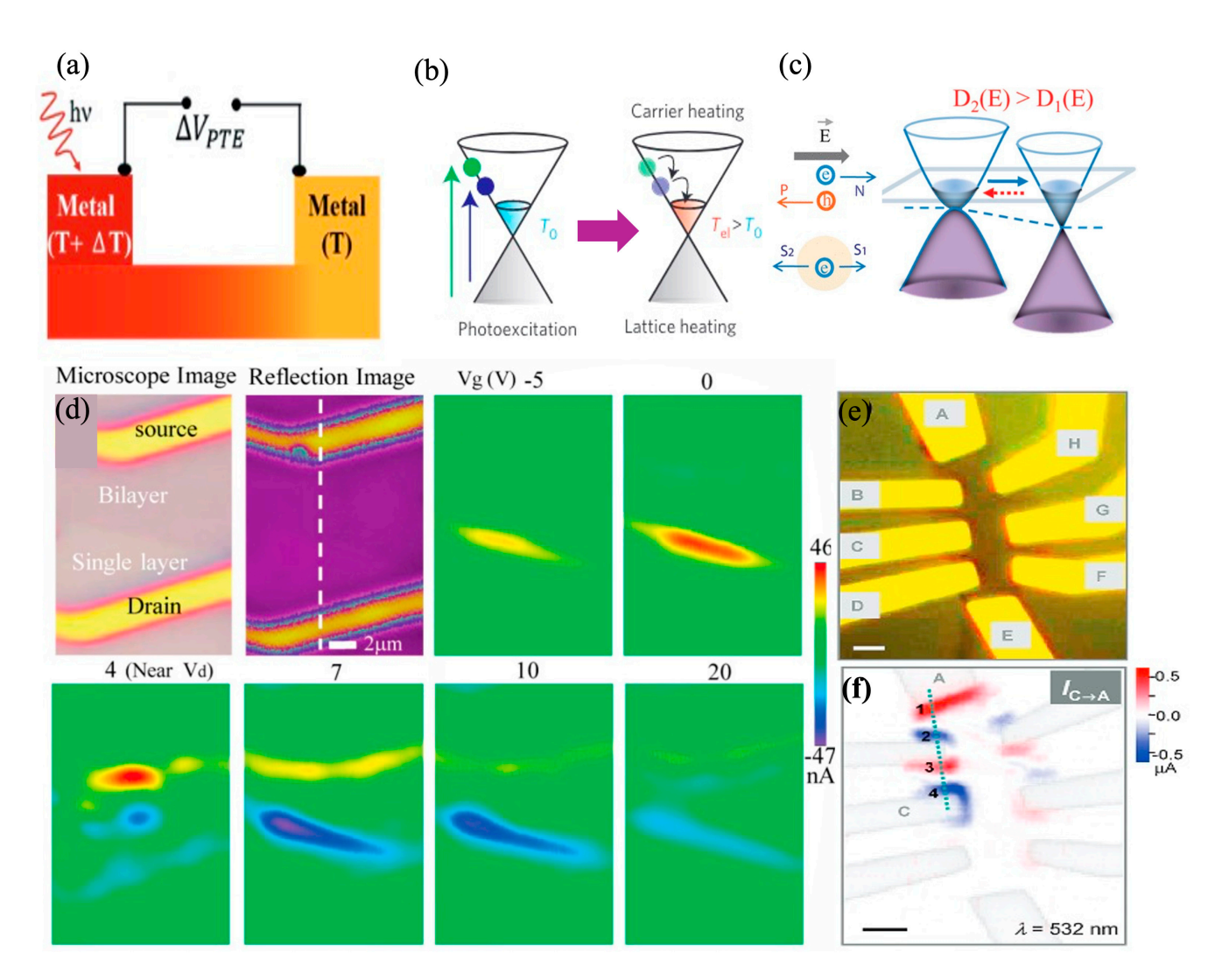


Figure 9. (a) Schematic diagram of photothermoelectric effect. Reproduced with permission [122]. Copyright 2021, Wiley–VCH. (b) After photoexcitation and electron–hole pair generation, electron heating and lattice heating take place. Carrier–carrier scattering leads to hot electrons which drive a photothermoelectric current. Reproduced with permission [123]. Copyright 2015, Springer Nature. (**c,d**) Photothermoelectric effect at a graphene interface junction. Reproduced with permission [128]. Copyright 2010, American Chemical Society. (**e,f**) Optical image and photocurrent imaging of a graphene device. Reproduced with permission [56]. Copyright 2009, American Chemical Society.

In contrast to the unipolar properties of MoS₂, WSe₂ displays bipolar characteristics [134] and can be utilized for creating a p–n homojunction. Groenendijk et al. [135] documented the photovoltaic and photothermoelectric effects at the WSe₂ homojunction interface, which are modulated by gate separation. As can be seen in Figure 11g–i, the I–V curve of the electrostatically doped p–n junction is rectified, and the photoresponse at this junction is cut off when the incident photon energy is less than the bandgap. Therefore, in a p–n structure, the photocurrent arises from the photovoltaic effect. In the case of a p–p junction, a substantial photocurrent signal can still be generated under global irradiation by sub–bandgap radiation, indicating the presence of the PTE effect (Figure 11i). The temperature difference arises from the nonuniform thickness of the WSe₂ flake. When illuminated above the bandgap, the photothermoelectric current in the p–p structure is approximately twice as much as the photovoltaic current in the p–n structure, as shown in Figure 11h. This suggests that the photothermoelectric effect can significantly impact photodetectors based on TMDs. The absence of a photothermoelectric response was attributed to the substantial tunneling resistance in the depletion region.

Processes 2024, 12, 1728 17 of 27

Low et al. [136] conducted an investigation into the origin of the light response in BP phototransistors. Thick BP film (≈100 nm) was utilized to enhance light absorption and carrier mobility. Based on the Mott formula, the extracted Seebeck coefficient is $\approx \!\! +60~\mu V~K^{-1}.$ The spatial photocurrent distribution under 532 nm illumination revealed that the maxima photocurrent occurs in the BP channel, away from the BP-metal interface, indicating a photothermoelectric mechanism in the absence of a bias voltage condition. The corresponding responsivity is about 20 mA W^{-1} . Subsequently, a single–pixel BP photodetector for thermal imaging was developed [137]. During testing, an object is scanned relative to a tightly focused laser beam, and the reflected light is collected by the BP photothermoelectric detector. Under 532 nm and 1550 nm illumination, the spatial resolutions are \approx 270 and \approx 720 nm, respectively, closely approaching the diffraction limit resolution. Yuan et al. [58] discovered that the photocurrent response at the BP-metal interface was primarily influenced by the PTE effect under zero or low source-drain voltage (|VSD| < 0.15 V), as the zero photoelectric flow near the channel center remained independent of polarity. We further investigated the optical response associated with intrinsic polarization. To eliminate the impact of electrode edge orientation, a toroidal metal electrode was utilized as a photocurrent collector (Figure 10a). Figure 10b,c display the polarization sensitive photodetector's photocurrent under light, with greater light polarization along the armchair direction. This photodetector is sensitive to a wide wavelength range, from 400 nm to 1700 nm. At a wavelength of 1200 nm, it achieves a response rate of 0.35 mA W^{-1} and an anisotropy ratio of 3.5. The response time is approximately 40 μs, limited by the measurement time resolution.

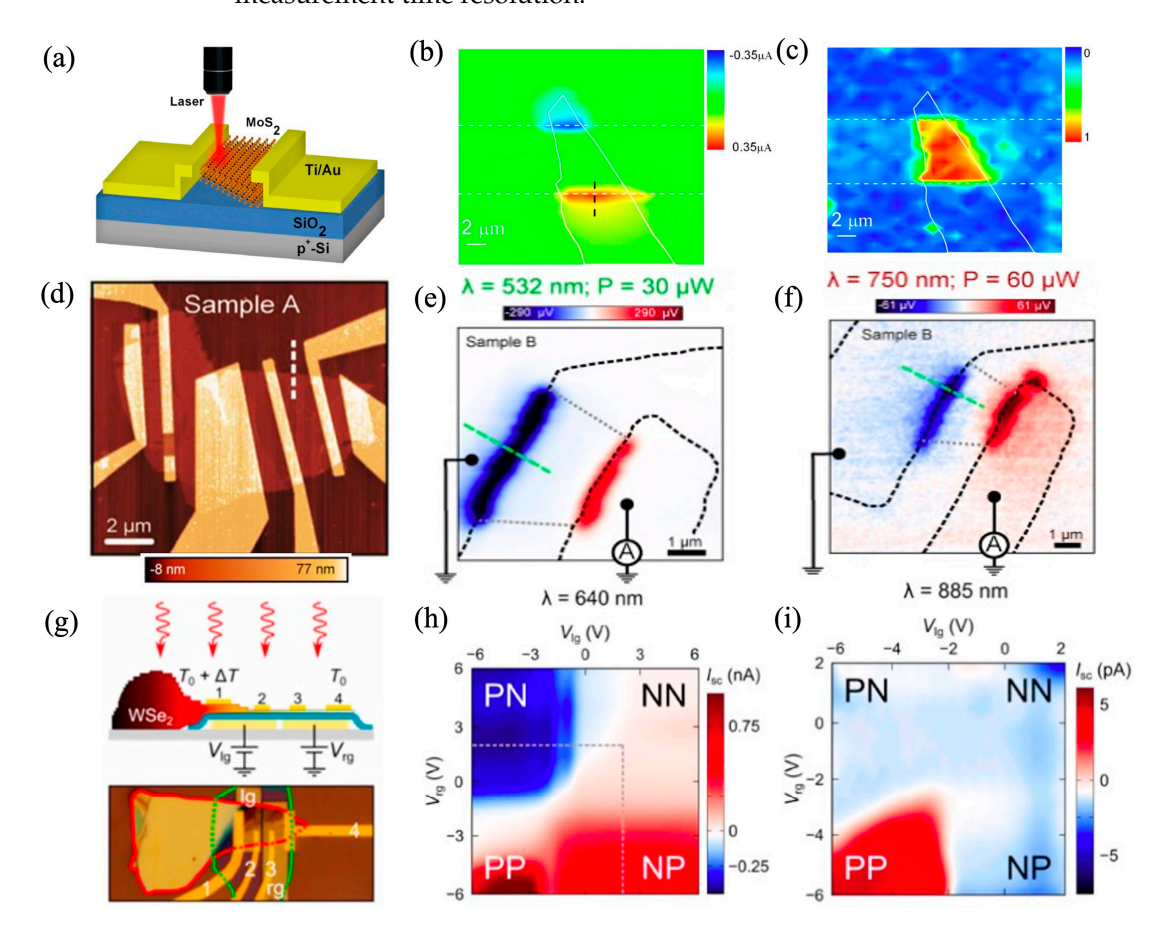


Figure 10. (a–c) Optical image and photocurrent microscopy image of a BP photodetector. Reproduced with permission [58]. Copyright 2015, Springer Nature. (**d**,**e**) Optical image and photoresponse of the TaIrTe₄ photodetector. Reproduced with permission [138]. Copyright 2018, American Chemical Society. (**f**,**g**) The performance of NdSb₂ photodetector. Reproduced with permission [139]. Copyright 2022, Springer Nature.

Processes 2024. 12. 1728 18 of 27

Chemical stability poses a significant challenge for BP photodetectors when they are subjected to ambient conditions, leading to a degradation in device performance and thereby limiting their practical utility. Therefore, various photothermoelectric photovoltaic devices based on 2D materials have been developed [39,138–140]. Lai et al. [138] demonstrated the development of a broad–spectrum self–powered photodetector using TaIrTe₄. The photocurrent generation mechanisms are investigated through the measurement of the photoresponse with respect to power and temperature. The metal–TaIrTe₄–metal photodetector displays a responsivity of 20 μ AW⁻¹ and a specific detectivity of 1.8 \times 10⁶ Jones with a 27 μ s response time at 10.6 μ m, as shown in Figure 10d,e. Li et al. [139] reported that the RSb₂ photodetector displays a responsivity of 0.49 mA·W⁻¹ with a 15 μ s response time at 532 nm and high stability under environmental conditions over 8 months. Furthermore, they conducted measurements on the polarization–sensitive light response of the detector, revealing an anisotropy coefficient as high as 1.6 (Figure 10f,g).

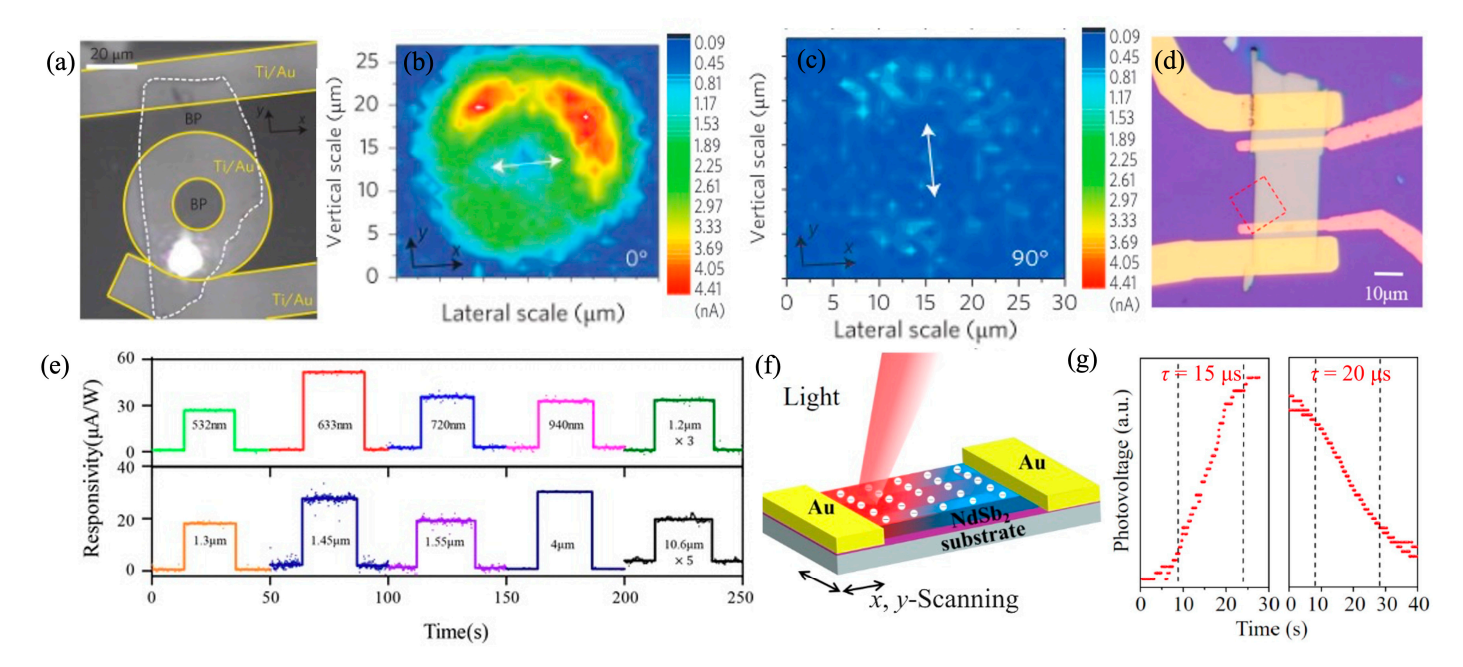


Figure 11. (**a**–**c**) Schematic illustration, photocurrent mapping, and Raman mapping of MoS₂. Reproduced with permission [132]. Copyright 2015, Springer Nature. (**d**–**f**) Photothermoelectric effect in monolayer MoS₂. Reproduced with permission [133]. Copyright 2013, American Chemical Society. (**g**–**i**) Photovoltaic and photothermoelectric effect in a double–gated WSe₂ device. Reproduced with permission [135]. Copyright 2014, American Chemical Society.

4. Comparisons and Perspectives

In Tables 1 and 2, we summarized the recently reported self–powered photodetectors and photovoltaic devices based on 2D materials and their performance parameters. The mechanism, working wavelength, on/off ratio, responsivity, photoresponse time, open voltage, short current, fill factor, and external quantum efficiency of optoelectronic devices are concluded and compared. As depicted in Tables 1 and 2, the currently reported self–powered photodetectors and photovoltaic devices can be classified into three types based on their working mechanisms: interface–junction optoelectronic devices, bulk photovoltaic effect optoelectronic devices, and photothermoelectric effect optoelectronic devices. Each of these device types possesses unique advantages but also comes with certain limitations. Interface–junction optoelectronic devices exhibit distinct photovoltaic properties, resulting in excellent light response. However, the construction of the interface junction is constrained by material type, and the open–circuit voltage is limited by semiconductor energy band. In contrast to interface–junction optoelectronic devices, bulk photovoltaic effect optoelectronic devices offer an open–circuit voltage that is not bound by semicon-

Processes 2024, 12, 1728 19 of 27

ductor bandgap limits. Furthermore, their power conversion efficiency has the potential to surpass the Shockley–Queisser limit. Nevertheless, their power conversion efficiency still lags behind that of interface–junction optoelectronic devices. Photothermoelectric effect optoelectronic devices demonstrate a broad–spectrum optical response without being restricted by material bandgap limits. Nonetheless, they suffer from slow responsiveness as compared to conventional photodetectors. In our Comparisons and Perspectives Section, we discuss strategies for further enhancing self–driven 2D–material–based solar cells.

Table 1. Recently reported self–powered photodetectors based on 2D materials and their performance parameters.

Mechanism	Device	Working Wavelength	I _{on} /I _{off}	Responsivity	Rise Time	Refs.
PV	p-GaTe/n-MoS ₂	633 nm	340	$1.36~{\rm A}~{ m W}^{-1}$	10 ms	
PV	$p-WS_2/n-MoS_2$	514 nm	-	$44~\mathrm{mA~W^{-1}}$	100 μs	[79]
PV	p-PtSe ₂ /n-Si	808 nm	1.5×10^{5}	$520 \mathrm{mA} \mathrm{W}^{-1}$	13.9 μs	[90]
PV	p–GaSe/n–InSe	470 nm	-	$21~\mathrm{mA~W^{-1}}$	1.85 µs	[32]
PV	Graphene p-n homojunction	633 nm	-	$5~\mathrm{mA~W^{-1}}$	0.9 ms	[142]
PV	$p-MoS_2/n-WS_2$	532 nm	10^{2}	$4.36 \mathrm{mA} \mathrm{W}^{-1}$	4 ms	[143]
PV	p-GaN/n-MoS ₂	550 nm	10^{5}	$443.3 \; \mathrm{A} \; \mathrm{W}^{-1}$	5 ms	[144]
PV	rGO/n–Si	600 nm	10^{4}	$1.52~{\rm A}~{ m W}^{-1}$	2 ms	[145]
PV	Au-InSe/Au-In	365 nm	10^{3}	369 mA W^{-1}	23 ms	[102]
PV	Au-BN/plasma Schottky contact	250 nm	350	$296 \mathrm{mA} \mathrm{W}^{-1}$	400 ms	[146]
PV	Au-MoS ₂ -ITO	637 nm	10^{6}	$1\mathrm{A}\mathrm{W}^{-1}$	64 μs	[103]
PV	Au-WSe ₂ -ITO	637 nm	10^{4}	$0.1~{ m A}~{ m W}^{-1}$	50 μs	[104]
PV	Graphene/ZnO:Al	380 nm	10^{2}	39 mA W^{-1}	37 μs	[147]
PV	Graphene/germanium	1550 nm	$2 imes 10^4$	$51.8 \mathrm{mA} \mathrm{W}^{-1}$	23 μs	[148]
PV	Graphene/Si	850 nm	10^{6}	29 mA W^{-1}	93 μs	[149]
PV	Graphene/GaAs	532 nm	-	231 mA W^{-1}	85 μs	[106]
PV	Si-QD/graphene/Si	860 nm	-	$495 \mathrm{mA} \mathrm{W}^{-1}$	25ns	[108]
BPVE	[CH ₃ (CH ₂) ₃ NH ₃] ₂ (CH ₃ NH ₃) Pb ₂ Br ₇	405 nm	1.2×10^3	-	20 μs	[150]
BPVE	Gr/ MoS ₂ /Gr	633 nm	-	$68 \ { m mA} \ { m W}^{-1}$	-	[57]
BPVE	Distorted MoTe ₂	400 nm	-	98 mA W^{-1}	-	[151]
BPVE	(allyammonium) ₂ (ethylammonium) ₂					
	Pb_3Br_{10}	405 nm	10^{4}	$50~\mu\mathrm{A}~\mathrm{W}^{-1}$	-	[152]
BPVE	$Sn_2P_2S_6$	405 nm	10^{3}	$3~\mathrm{mA~W^{-1}}$	230 ms	[153]
PTE	Graphene (asymmetric electrodes)	1.54, 119 μm	-	$0.25, 10 \mathrm{V} \ \mathrm{W}^{-1}$	110 ps	[154]
PTE	Graphene/SiN	10.6 μm	-	$7-9 \text{ V W}^{-1}$	23 ms	[155]
PTE	Graphene/SiO ₂	6.4–10 μm	-	$78\mathrm{nA}~\mathrm{W}^{-1}$	-	[156]
PTE	Graphene (antenna–assisted)	157 μm	-	$4.9~{ m V}~{ m W}^{-1}$	-	[157]
PTE	Black phosphorus	400–1700 nm	-	$0.35 \mathrm{mA} \mathrm{W}^{-1}$	40 μs	[58]
PTE	BP (antenna–assisted)	1.006 mm	-	$0.15~{ m V}~{ m W}^{-1}$	-	[158]
PTE	Carbon nanotube film	660 nm	-	$45~\mathrm{mA~W^{-1}}$	80 μs	[159]
PTE	Carbon nanotube film	215, 119, 96 μm	-	$2.5, 1, 7 \text{ V W}^{-1}$	-	[160]
PTE	GaN/AlGaN/GaN nanowire	325 nm	-		<30 ms	[161]
PTE	Nanoporous silicon	660 nm	-	-	5 s	[162]

The term "IoT battery" has gained popularity in the energy sector, highlighting the importance of energy storage/conversion devices as an indispensable power source for various IoT devices, robotic devices, and mobile AI devices. Self–powered energy–driven optoelectronic devices have become significantly important in recent years. To achieve this goal, innovatively designed 2D self–powered optoelectronic devices offer a highly promising platform. To promote the further applications of the self–powered photoelectric devices based on 2D materials in the field of IoT, we propose possible future directions and challenges are highlighted. (1) Due to the small built–in electric field between conventional homojunction and heterojunction materials, a small photocurrent results. Identifying novel and effective approaches to enhance the size of the built–in electric field of p–n junctions and Schottky junctions is also a viable method for further enhancing the performance of self–powered photoelectric devices. For example, such strategies can be achieved by searching for a more matched combination of light–absorbing materials, constructing p–n

Processes 2024, 12, 1728 20 of 27

junctions or Schottky junctions with powerful built-in electric fields, or by improving their built-in electric fields by more efficient modification means. (2) Currently, the 2D material BPVE is only found in 20 non-centrosymmetric structural point groups, which limits the number of material systems that can be developed. However, in the future, by breaking the spatial inversion symmetry through external action, it is crucial to expand the material crystal types to 32 crystal point groups. (3) Compared with traditional self-powered optoelectronics, fabricating large-scale 2D materials with high quality remains challenging, yet they are essential for practical optoelectronic devices. Future research should prioritize developing large-scale production methods to enable practical low-power applications in IoT and electronics. (4) The integration of wearable health management components with self-powered DC power supplies is a crucial application. Specifically, flexible self-powered photoelectric devices that are stretchable, biocompatible, and inexpensive to produce enable the real-time continuous monitoring of medical devices. Overall, our review on self-powered optoelectronic 2D devices paves the way for designing novel devices with better integration and "all-in-one" multifunctionality.

Table 2. Recently reported self–powered photovoltaic devices based on 2D materials and their performance parameters.

Mechanism	Device	$V_{oc}[V]$	I_{sc} or J_{sc}	FF	PCE	QE (%)	Refs.
PV	Mo _{0.5} W _{0.5} Se ₂	0.44	92 mA cm ⁻²	0.32	5–16	=	[163]
PV	WSe ₂	0.65	1 nA	-	0.005	0.2 (EQE)	[164]
PV	BP (6 nm)	0.05	1 nA	0.3	< 0.001	0.1 (EQE)	[165]
PV	MoSe ₂	0.36	0.6 nA	0.7	14	-	[166]
PV	BP (8.5 nm)	0.14	3 nA	0.38	0.66	-	[31]
PV	BP (2.8 nm)	0.44	180 nA	0.75	0.75	-	[81]
PV	WS_2 - WSe_2	0.47	1.2 nA	-	0.9	43 (IQE)	[68]
PV	WSe_2-MoS_2	0.22	0.008 nA	0.39	0.2	-	[82]
PV	MoS_2	0.28	20.9 mA cm^{-2}	0.47	2.8	37-78 (EQE)	[131]
PV	BP/MoS_2	0.3	20 nA	0.5	0.57	0.3 (EQE)	[45]
PV	ML WSe ₂ /FL MoS ₂	0.27	200 nA	0.4	12	-	[79]
PV	ML WSe ₂ /MoS ₂	0.53	0.005 nA	-	0.2	1.5 (EQE)	[84]
PV	MoS ₂ /Si	0.41	22.36 mA cm^{-2}	0.57	5.23	-	[167]
PV	MoS ₂ /h-BN/GaAs	0.76	21.1 mA cm^{-2}	-	9.03	56.3 (EQE)	[168]
PV	MoS ₂ /InP	0.47	27.4 A cm^{-2}	0.55	7.1	-	[169]
PV	Gr/MoS ₂ /Gr	0.28	1700 nA	_	-	85 (IQE)	[170]
PV	MoSe2/GaN	0.62	6.05 mA cm^{-2}	0.35	1.29	-	[171]
PV	GQDs/MoS ₂ /InP	0.27	24.2 mA cm^{-2}	0.53	4.1	-	[172]
PV	Gr/GaAs	0.81	24.9 mA cm^{-2}	0.69	16.2	_	[173]
PV	$MoS_2/SiO_2/p$ -Si	0.3	5.5 mA cm^{-2}	0.42	4.5	_	[174]
PV	BP/GaAs	0.6	1250 nA	0.3	0.24	31 (EOE)	[175]
BPVE	Nanotube WS ₂	0.35	15 nA	-	-	1.3 (EQE)	[116]
BPVE	CuInP ₂ S ₆	0.8	$10 \mathrm{\ mA\ cm^{-2}}$	25	0.02	-	[117]
BPVE	BiFeO ₃	0.27	$3.8 \times 10^{-7} \text{ A cm}^{-2}$	25	0.0034	_	[176]
BPVE	BaTiO ₃ (20 nm)	0.6	$2.2 \times 10^{-6} \text{ A cm}^{-2}$	25	< 0.001	_	[177]
BPVE	KBNNO	3.5	$4 \times 10^{-8} \text{ A cm}^{-2}$	31.5	0.0011	_	[178]
BPVE	PLZTN	23	$3.7 \times 10^{-8} \text{ A cm}^{-2}$	46	< 0.001	_	[44]
BPVE	BBLT	16	$6.5 \times 10^{-9} \text{ A cm}^{-2}$	29	< 0.001	_	[179]
BPVE	hBN/Gr/3RMoS ₂ /Gr/hBN/Gr	0.06	30 nA	-	-	16 (EQE)	[118]
BPVE	Strained MoS ₂	0.003	20 nA	_	_	- (- 2 -)	[55]
BPVE	Gr/MoS ₂ /Gr	0.1	1.0 μΑ	_	_	2.5 (EQE)	[57]
BPVE	Distorted MoTe ₂	0.016	60 μΑ	-	-	30 (EQE)	[151]
BPVE	$MASnI_3$	0.57	12.47 mA cm^{-2}	0.44	3.13	-	[180]
BPVE	FASnI ₃	0.64	25.36 mA cm ⁻²	0.56	5.51	-	[180]
BPVE	(allyammnium) ₂ (ethylammonium) ₂						[-50]
	Pb ₃ Br ₁₀	2.5	5 nA	_	-	-	[152]
BPVE	$Sn_2P_2S_6$	0.16	1.1 mA cm ⁻²	_	-	0.8 (EQE)	[153]
PTE	Carbon nanotube film	0.002	25 μΑ	_	-	-	[159]
PTE	Carbon nanotube film	0.0004	3 nA	_	_	_	[162]

5. Summary

With the advent of the post–Moore era and the rapid advancement of the semiconductor industry, low–power self–powered devices have become an essential component of electronic and optoelectronic products. Self–powered optoelectronic devices based on 2D materials have been extensively researched for their exceptional performance and unique application scenarios, thus becoming a crucial element within this field. In this review, we comprehensively summarize the latest research progress of 2D–material–based self–powered photoelectric devices. The fascinating properties of two–dimensional materi-

Processes 2024, 12, 1728 21 of 27

als render them promising candidates for future photoelectric applications. We summarize three photoelectric conversion mechanisms based on self–powered photoelectric devices: the interface–junction effect, the bulk photovoltaic effect, and the photothermoelectric effect. This serves to provide readers from various disciplines with a comprehensive understanding of the numerous studies conducted on self–powered optoelectronic devices utilizing 2D materials.

Author Contributions: Conceptualization, Z.Z., W.Z. and Z.C.; writing—original draft preparation, J.X.; writing—review and editing, Z.Z., W.Z. and Z.C.; supervision, Z.Z. All authors have read and agreed to the published version of the manuscript.

Funding: This research was funded by the Postgraduate Research & Practice Innovation Program of Jiangsu Province (KYCX24_0658).

Acknowledgments: We acknowledge financial support from Nanjing University of Science and Technology (AE899991/406, AD411203).

Conflicts of Interest: The authors declare no conflicts of interest.

References

- 1. Khatua, P.K.; Ramachandaramurthy, V.K.; Kasinathan, P.; Yong, J.Y.; Pasupuleti, J.; Rajagopalan, A. Application and Assessment of Internet of Things toward the Sustainability of Energy Systems: Challenges and Issues. *Sustain. Cities Soc.* **2020**, *53*, 101957. [CrossRef]
- Salam, A. Internet of Things for Sustainable Community Development: Wireless Communications, Sensing, and Systems; Springer International Publishing: Cham, Switzerland, 2020; ISBN 978-3-030-35290-5.
- 3. Sun, Y.; Wu, Q.; Shi, G. Graphene Based New Energy Materials. Energy Environ. Sci. 2011, 4, 1113. [CrossRef]
- 4. Feng, J.; Wang, Y.; Xu, Y.; Sun, Y.; Tang, Y.; Yan, X. Ion Regulation of Ionic Liquid Electrolytes for Supercapacitors. *Energy Environ. Sci.* **2021**, *14*, 2859–2882. [CrossRef]
- 5. Jayakody, D.N.K.; Thompson, J.; Chatzinotas, S.; Durrani, S. (Eds.) Wireless Information and Power Transfer: A New Paradigm for Green Communications; Springer International Publishing: Cham, Switzerland, 2018; ISBN 978-3-319-56668-9.
- 6. Hatch, S.M.; Briscoe, J.; Dunn, S. A Self-Powered ZnO-Nanorod/CuSCN UV Photodetector Exhibiting Rapid Response. *Adv. Mater.* **2013**, 25, 867–871. [CrossRef] [PubMed]
- 7. Yang, Y.; Guo, W.; Qi, J.; Zhao, J.; Zhang, Y. Self-Powered Ultraviolet Photodetector Based on a Single Sb-Doped ZnO Nanobelt. *Appl. Phys. Lett.* **2010**, 97, 223113. [CrossRef]
- 8. Xie, Y.; Wei, L.; Wei, G.; Li, Q.; Wang, D.; Chen, Y.; Yan, S.; Liu, G.; Mei, L.; Jiao, J. A Self-Powered UV Photodetector Based on TiO₂ Nanorod Arrays. *Nanoscale Res. Lett.* **2013**, *8*, 188. [CrossRef] [PubMed]
- 9. Hou, X.; Wang, X.; Liu, B.; Wang, Q.; Wang, Z.; Chen, D.; Shen, G. SnO₂ @TiO₂ Heterojunction Nanostructures for Lithium-Ion Batteries and Self-Powered UV Photodetectors with Improved Performances. *ChemElectroChem* **2014**, *1*, 108–115. [CrossRef]
- 10. Hu, J.; Zhang, Y.; Sun, M.; Piedra, D.; Chowdhury, N.; Palacios, T. Materials and Processing Issues in Vertical GaN Power Electronics. *Mater. Sci. Semicon. Proc.* **2018**, *78*, 75–84. [CrossRef]
- 11. Flack, T.J.; Pushpakaran, B.N.; Bayne, S.B. GaN Technology for Power Electronic Applications: A Review. *J. Electron. Mater.* **2016**, 45, 2673–2682. [CrossRef]
- 12. Li, P.; Zhang, Z.; Shen, W.; Hu, C.; Shen, W.; Zhang, D. A Self-Powered 2D-Material Sensor Unit Driven by a SnSe Piezoelectric Nanogenerator. *J. Mater. Chem. A* **2021**, *9*, 4716–4723. [CrossRef]
- 13. Li, P.; Zhang, Z. Self-Powered 2D Material-Based pH Sensor and Photodetector Driven by Monolayer MoSe₂ Piezoelectric Nanogenerator. *ACS Appl. Mater. Interfaces* **2020**, *12*, 58132–58139. [CrossRef]
- 14. Wu, E.; Wu, D.; Jia, C.; Wang, Y.; Yuan, H.; Zeng, L.; Xu, T.; Shi, Z.; Tian, Y.; Li, X. In Situ Fabrication of 2D WS₂ /Si Type-II Heterojunction for Self-Powered Broadband Photodetector with Response up to Mid-Infrared. *ACS Photonics* **2019**, *6*, 565–572. [CrossRef]
- 15. Novoselov, K.S.; Geim, A.K.; Morozov, S.V.; Jiang, D.; Zhang, Y.; Dubonos, S.V.; Grigorieva, I.V.; Firsov, A.A. Electric Field Effect in Atomically Thin Carbon Films. *Science* **2004**, *306*, 666–669. [CrossRef] [PubMed]
- 16. Li, L.; Yu, Y.; Ye, G.J.; Ge, Q.; Ou, X.; Wu, H.; Feng, D.; Chen, X.H.; Zhang, Y. Black Phosphorus Field-Effect Transistors. *Nat. Nanotechnol.* **2014**, *9*, 372–377. [CrossRef] [PubMed]
- 17. Lu, S.B.; Miao, L.L.; Guo, Z.N.; Qi, X.; Zhao, C.J.; Zhang, H.; Wen, S.C.; Tang, D.Y.; Fan, D.Y. Broadband Nonlinear Optical Response in Multi-Layer Black Phosphorus: An Emerging Infrared and Mid-Infrared Optical Material. *Opt. Express* 2015, 23, 11183. [CrossRef] [PubMed]
- 18. Liu, L.; Feng, Y.P.; Shen, Z.X. Structural and Electronic Properties of h -BN. Phys. Rev. B 2003, 68, 104102. [CrossRef]
- 19. Wang, S.; Wang, X.; Warner, J.H. All Chemical Vapor Deposition Growth of MoS₂: H-BN Vertical van Der Waals Heterostructures. *ACS Nano* **2015**, *9*, 5246–5254. [CrossRef]

Processes **2024**, 12, 1728 22 of 27

20. Mukundan, A.; Feng, S.-W.; Weng, Y.-H.; Tsao, Y.-M.; Artemkina, S.B.; Fedorov, V.E.; Lin, Y.-S.; Huang, Y.-C.; Wang, H.-C. Optical and Material Characteristics of MoS₂/Cu₂O Sensor for Detection of Lung Cancer Cell Types in Hydroplegia. *Int. J. Mol. Sci.* 2022, 23, 4745. [CrossRef] [PubMed]

- 21. Lee, C.; Yan, H.; Brus, L.E.; Heinz, T.F.; Hone, J.; Ryu, S. Anomalous Lattice Vibrations of Single- and Few-Layer MoS₂. ACS Nano 2010, 4, 2695–2700. [CrossRef]
- 22. Splendiani, A.; Sun, L.; Zhang, Y.; Li, T.; Kim, J.; Chim, C.-Y.; Galli, G.; Wang, F. Emerging Photoluminescence in Monolayer MoS₂. *Nano Lett.* **2010**, *10*, 1271–1275. [CrossRef]
- 23. Chen, Z.; Biscaras, J.; Shukla, A. Optimal Light Harvesting in 2D Semiconductor Heterostructures. 2d Mater. 2017, 4, 025115. [CrossRef]
- 24. Lai, C.-L.; Karmakar, R.; Tsao, Y.-M.; Lu, S.-C.; Mukundan, A.; Liu, P.-H.; Wang, H.-C. Fabrication of MoS₂ Nanoparticle Dispersions Using Ultrasonic Methods: Synthesis Techniques and Optical Characterization. *Opt. Mater. Express* **2024**, *14*, 2003–2016. [CrossRef]
- 25. Mukundan, A.; Tsao, Y.-M.; Artemkina, S.B.; Fedorov, V.E.; Wang, H.-C. Growth Mechanism of Periodic-Structured MoS₂ by Transmission Electron Microscopy. *Nanomaterials* **2021**, *12*, 135. [CrossRef]
- 26. Lai, C.-L.; Karmakar, R.; Mukundan, A.; Chen, W.-C.; Wu, I.-C.; Fedorov, V.E.; Feng, S.-W.; Choomjinda, U.; Huang, S.-F.; Wang, H.-C. Lung Cancer Cells Detection by a Photoelectrochemical MoS₂ Biosensing Chip. *Biomed. Opt. Express* **2024**, *15*, 753. [CrossRef]
- 27. Ernandes, C.; Khalil, L.; Almabrouk, H.; Pierucci, D.; Zheng, B.; Avila, J.; Dudin, P.; Chaste, J.; Oehler, F.; Pala, M.; et al. Indirect to Direct Band Gap Crossover in Two-Dimensional WS₂(1–x)Se₂x Alloys. *NPJ 2d Mater. Appl.* **2021**, *5*, 7. [CrossRef]
- 28. Li, Y.; Ding, T.; Sang, D.K.; Wu, M.; Li, J.; Wang, C.; Liu, F.; Zhang, H.; Xie, H. Evolutional Carrier Mobility and Power Factor of Two-Dimensional Tin Telluride Due to Quantum Size Effects. *J. Mater. Chem. C* **2020**, *8*, 4181–4191. [CrossRef]
- 29. Novoselov, K.S.; Mishchenko, A.; Carvalho, A.; Castro Neto, A.H. 2D Materials and van Der Waals Heterostructures. *Science* **2016**, 353, aac9439. [CrossRef]
- 30. Kim, Y.; Lee, S.; Song, J.; Ko, K.Y.; Woo, W.J.; Lee, S.W.; Park, M.; Lee, H.; Lee, Z.; Choi, H.; et al. 2D Transition Metal Dichalcogenide Heterostructures for P-and n-Type Photovoltaic Self-Powered Gas Sensor. *Adv. Funct. Mater.* **2020**, *30*, 2003360. [CrossRef]
- 31. Liu, Y.; Cai, Y.; Zhang, G.; Zhang, Y.; Ang, K. Al-Doped Black Phosphorus p–n Homojunction Diode for High Performance Photovoltaic. *Adv. Funct. Mater.* **2017**, 27, 1604638. [CrossRef]
- 32. Yan, F.; Zhao, L.; Patanè, A.; Hu, P.; Wei, X.; Luo, W.; Zhang, D.; Lv, Q.; Feng, Q.; Shen, C.; et al. Fast, Multicolor Photodetection with Graphene-Contacted *p*-GaSe/ *n*-InSe van Der Waals Heterostructures. *Nanotechnology* **2017**, *28*, 27LT01. [CrossRef]
- 33. Zheng, W.; Zheng, B.; Yan, C.; Liu, Y.; Sun, X.; Qi, Z.; Yang, T.; Jiang, Y.; Huang, W.; Fan, P.; et al. Direct Vapor Growth of 2D Vertical Heterostructures with Tunable Band Alignments and Interfacial Charge Transfer Behaviors. *Adv. Sci.* **2019**, *6*, 1802204. [CrossRef] [PubMed]
- 34. Jariwala, D.; Marks, T.J.; Hersam, M.C. Mixed-Dimensional van Der Waals Heterostructures. *Nat. Mater.* **2017**, *16*, 170–181. [CrossRef] [PubMed]
- 35. Guo, T.; Song, X.; Wei, P.; Li, J.; Gao, Y.; Cheng, Z.; Zhou, W.; Gu, Y.; Chen, X.; Zeng, H.; et al. High-Gain MoS₂/Ta₂ NiSe₅ Heterojunction Photodetectors with Charge Transfer and Suppressing Dark Current. *ACS Appl. Mater. Interfaces* **2022**, *14*, 56384–56394. [CrossRef] [PubMed]
- 36. Wu, F.; Tian, H.; Yan, Z.; Ren, J.; Hirtz, T.; Gou, G.; Shen, Y.; Yang, Y.; Ren, T.-L. Gate-Tunable Negative Differential Resistance Behaviors in a hBN-Encapsulated BP-MoS₂ Heterojunction. *ACS Appl. Mater. Interfaces* **2021**, *13*, 26161–26169. [CrossRef] [PubMed]
- 37. Chen, Z.; Biscaras, J.; Shukla, A. A High Performance Graphene/Few-Layer InSe Photo-Detector. *Nanoscale* **2015**, *7*, 5981–5986. [CrossRef] [PubMed]
- 38. Chen, Z. A High Performance Self-Driven Photodetector Based on a Graphene/InSe/MoS₂ Vertical Heterostructure. *J. Mater. Chem. C* **2018**, *6*, 12407–12412. [CrossRef]
- 39. Lu, X.; Jiang, P.; Bao, X. Phonon-Enhanced Photothermoelectric Effect in SrTiO₃ Ultra-Broadband Photodetector. *Nat. Commun.* **2019**, *10*, 138. [CrossRef] [PubMed]
- Buscema, M.; Island, J.O.; Groenendijk, D.J.; Blanter, S.I.; Steele, G.A.; Van Der Zant, H.S.J.; Castellanos-Gomez, A. Photocurrent Generation with Two-Dimensional van Der Waals Semiconductors. *Chem. Soc. Rev.* 2015, 44, 3691–3718. [CrossRef] [PubMed]
- 41. Yadav, A.; Vashishtha, P.; Goswami, L.; Kumari, P.; Khan, A.; Yadav, R.; Sharma, A.; Prajapat, P.; Gupta, G. Plasmonics Stimulated Enhanced Performance MoS₂/WO₃ Heterojunction Based Broadband Self-Powered Photodetector. *ACS Appl. Opt. Mater.* **2024**, 2, 784–794. [CrossRef]
- 42. Yao, J.D.; Shao, J.M.; Li, S.W.; Bao, D.H.; Yang, G.W. Polarization Dependent Photocurrent in the Bi₂Te₃ Topological Insulator Film for Multifunctional Photodetection. *Sci. Rep.* **2015**, *5*, 14184. [CrossRef] [PubMed]
- 43. Xu, K. Silicon electro-optic micro-modulator fabricated in standard CMOS technology as components for all silicon monolithic integrated optoelectronic systems. *J. Micromech. Microeng.* **2021**, *31*, 054001. [CrossRef]
- 44. Huangfu, G.; Xiao, H.; Guan, L.; Zhong, H.; Hu, C.; Shi, Z.; Guo, Y. Visible or Near-Infrared Light Self-Powered Photodetectors Based on Transparent Ferroelectric Ceramics. *ACS Appl. Mater. Interfaces* **2020**, 12, 33950–33959. [CrossRef]

Processes **2024**, 12, 1728 23 of 27

45. Deng, Y.; Luo, Z.; Conrad, N.J.; Liu, H.; Gong, Y.; Najmaei, S.; Ajayan, P.M.; Lou, J.; Xu, X.; Ye, P.D. Black Phosphorus–Monolayer MoS₂ van Der Waals Heterojunction p–n Diode. *ACS Nano* **2014**, *8*, 8292–8299. [CrossRef]

- 46. Dai, M.; Wu, Q.; Wang, C.; Liu, X.; Zhang, X.; Cai, Z.; Lin, L.; Gu, X.; Ostrikov, K.; Nan, H.; et al. High Performance Self-Driven Photodetectors Based on MoS₂ Schottky Barrier Diode. *Adv. Opt. Mater.* **2024**, *12*, 2301900. [CrossRef]
- 47. Long, M.; Wang, P.; Fang, H.; Hu, W. Progress, Challenges, and Opportunities for 2D Material Based Photodetectors. *Adv. Funct. Mater.* **2019**, 29, 1803807. [CrossRef]
- 48. Hu, C.; Wang, X.; Song, B. High-Performance Position-Sensitive Detector Based on the Lateral Photoelectrical Effect of Two-Dimensional Materials. *Light. Sci. Appl.* **2020**, *9*, 88. [CrossRef]
- 49. Wang, L.; Huang, L.; Tan, W.C.; Feng, X.; Chen, L.; Ang, K. Pronounced Photovoltaic Effect in Electrically Tunable Lateral Black-Phosphorus Heterojunction Diode. *Adv. Elect. Mater.* **2018**, *4*, 1700442. [CrossRef]
- 50. Jin, Y.; Keum, D.H.; An, S.; Kim, J.; Lee, H.S.; Lee, Y.H. A Van Der Waals Homojunction: Ideal p–n Diode Behavior in MoSe₂. *Adv. Mater.* **2015**, 27, 5534–5540. [CrossRef]
- 51. Zhou, C.; Raju, S.; Li, B.; Chan, M.; Chai, Y.; Yang, C.Y. Self-Driven Metal–Semiconductor–Metal WSe₂ Photodetector with Asymmetric Contact Geometries. *Adv. Funct. Mater.* **2018**, *28*, 1802954. [CrossRef]
- 52. Butler, K.T.; Frost, J.M.; Walsh, A. Ferroelectric Materials for Solar Energy Conversion: Photoferroics Revisited. *Energy Environ. Sci.* **2015**, *8*, 838–848. [CrossRef]
- 53. Akamatsu, T.; Ideue, T.; Zhou, L.; Dong, Y.; Kitamura, S.; Yoshii, M.; Yang, D.; Onga, M.; Nakagawa, Y.; Watanabe, K.; et al. A van Der Waals Interface That Creates In-Plane Polarization and a Spontaneous Photovoltaic Effect. *Science* **2021**, *372*, 68–72. [CrossRef]
- 54. Song, T.; Anderson, E.; Tu, M.W.-Y.; Seyler, K.; Taniguchi, T.; Watanabe, K.; McGuire, M.A.; Li, X.; Cao, T.; Xiao, D.; et al. Spin Photovoltaic Effect in Magnetic van Der Waals Heterostructures. *Sci. Adv.* **2021**, *7*, eabg8094. [CrossRef]
- 55. Jiang, J.; Chen, Z.; Hu, Y.; Xiang, Y.; Zhang, L.; Wang, Y.; Wang, G.-C.; Shi, J. Flexo-Photovoltaic Effect in MoS₂. *Nat. Nanotechnol.* **2021**, *16*, 894–901. [CrossRef]
- 56. Park, J.; Ahn, Y.H.; Ruiz-Vargas, C. Imaging of Photocurrent Generation and Collection in Single-Layer Graphene. *Nano Lett.* **2009**, *9*, 1742–1746. [CrossRef]
- 57. Yu, W.J.; Vu, Q.A.; Oh, H.; Nam, H.G.; Zhou, H.; Cha, S.; Kim, J.-Y.; Carvalho, A.; Jeong, M.; Choi, H.; et al. Unusually Efficient Photocurrent Extraction in Monolayer van Der Waals Heterostructure by Tunnelling through Discretized Barriers. *Nat. Commun.* **2016**, 7, 13278. [CrossRef] [PubMed]
- 58. Yuan, H.; Liu, X.; Afshinmanesh, F.; Li, W.; Xu, G.; Sun, J.; Lian, B.; Curto, A.G.; Ye, G.; Hikita, Y.; et al. Polarization-Sensitive Broadband Photodetector Using a Black Phosphorus Vertical p–n Junction. *Nat. Nanotechnol.* **2015**, *10*, 707–713. [CrossRef]
- 59. Adams, M.J.; Verosky, M.; Zebarjadi, M.; Heremans, J.P. High Switching Ratio Variable-Temperature Solid-State Thermal Switch Based on Thermoelectric Effects. *Int. J. Heat Mass Transf.* **2019**, *134*, 114–118. [CrossRef]
- 60. Dhanabalan, S.C.; Ponraj, J.S.; Zhang, H.; Bao, Q. Present Perspectives of Broadband Photodetectors Based on Nanobelts, Nanoribbons, Nanosheets and the Emerging 2D Materials. *Nanoscale* **2016**, *8*, 6410–6434. [PubMed]
- 61. Qi, B.; Wang, J. Open-Circuit Voltage in Organic Solar Cells. J. Mater. Chem. 2012, 22, 24315. [CrossRef]
- 62. He, Z.; Zhong, C.; Huang, X.; Wong, W.; Wu, H.; Chen, L.; Su, S.; Cao, Y. Simultaneous Enhancement of Open-Circuit Voltage, Short-Circuit Current Density, and Fill Factor in Polymer Solar Cells. *Adv. Mater.* **2011**, 23, 4636–4643. [CrossRef]
- 63. Jao, M.-H.; Liao, H.-C.; Su, W.-F. Achieving a High Fill Factor for Organic Solar Cells. J. Mater. Chem. A 2016, 4, 5784–5801.
- 64. Ting, C.-C.; Chao, W.-S. Measuring Temperature Dependence of Photoelectric Conversion Efficiency with Dye-Sensitized Solar Cells. *Measurement* **2010**, *43*, 1623–1627. [CrossRef]
- 65. Lin, K.; Xing, J.; Quan, L.N.; De Arquer, F.P.G.; Gong, X.; Lu, J.; Xie, L.; Zhao, W.; Zhang, D.; Yan, C.; et al. Perovskite Light-Emitting Diodes with External Quantum Efficiency Exceeding 20 percent. *Nature* 2018, 562, 245–248. [CrossRef] [PubMed]
- 66. Yang, W.J.; Ma, Z.Q.; Tang, X.; Feng, C.B.; Zhao, W.G.; Shi, P.P. Internal Quantum Efficiency for Solar Cells. *Sol. Energy* **2008**, *82*, 106–110. [CrossRef]
- 67. Bullock, J.; Amani, M.; Cho, J.; Chen, Y.-Z.; Ahn, G.H.; Adinolfi, V.; Shrestha, V.R.; Gao, Y.; Crozier, K.B.; Chueh, Y.-L.; et al. Polarization-Resolved Black Phosphorus/Molybdenum Disulfide Mid-Wave Infrared Photodiodes with High Detectivity at Room Temperature. *Nat. Photon.* 2018, 12, 601–607. [CrossRef]
- 68. Duan, X.; Wang, C.; Shaw, J.C.; Cheng, R.; Chen, Y.; Li, H.; Wu, X.; Tang, Y.; Zhang, Q.; Pan, A.; et al. Lateral Epitaxial Growth of Two-Dimensional Layered Semiconductor Heterojunctions. *Nat. Nanotechnol.* **2014**, *9*, 1024–1030. [CrossRef]
- 69. Huang, C.; Wu, S.; Sanchez, A.M.; Peters, J.J.P.; Beanland, R.; Ross, J.S.; Rivera, P.; Yao, W.; Cobden, D.H.; Xu, X. Lateral Heterojunctions within Monolayer MoSe₂–WSe₂ Semiconductors. *Nat. Mater.* **2014**, *13*, 1096–1101. [CrossRef] [PubMed]
- 70. Li, M.; Pu, J.; Huang, J.; Miyauchi, Y.; Matsuda, K.; Takenobu, T.; Li, L. Self-Aligned and Scalable Growth of Monolayer WSe₂ –MoS₂ Lateral Heterojunctions. *Adv. Funct. Mater.* **2018**, 28, 1706860. [CrossRef]
- 71. Xue, Y.; Zhang, Y.; Liu, Y.; Liu, H.; Song, J.; Sophia, J.; Liu, J.; Xu, Z.; Xu, Q.; Wang, Z.; et al. Scalable Production of a Few-Layer MoS₂ /WS₂ Vertical Heterojunction Array and Its Application for Photodetectors. *ACS Nano* **2016**, *10*, 573–580. [CrossRef]
- 72. Yang, T.; Zheng, B.; Wang, Z.; Xu, T.; Pan, C.; Zou, J.; Zhang, X.; Qi, Z.; Liu, H.; Feng, Y.; et al. Van Der Waals Epitaxial Growth and Optoelectronics of Large-Scale WSe₂/SnS₂ Vertical Bilayer p–n Junctions. *Nat. Commun.* **2017**, *8*, 1906. [PubMed]
- 73. Kufer, D.; Nikitskiy, I.; Lasanta, T.; Navickaite, G.; Koppens, F.H.L.; Konstantatos, G. Hybrid 2D–0D MoS₂–PbS Quantum Dot Photodetectors. *Adv. Mater.* **2015**, *27*, 176–180. [CrossRef] [PubMed]

Processes **2024**, 12, 1728 24 of 27

74. Mouafo, L.D.N.; Godel, F.; Melinte, G.; Hajjar-Garreau, S.; Majjad, H.; Dlubak, B.; Ersen, O.; Doudin, B.; Simon, L.; Seneor, P.; et al. Anisotropic Magneto-Coulomb Properties of 2D–0D Heterostructure Single Electron Device. *Adv. Mater.* **2018**, *30*, 1802478. [CrossRef]

- 75. Liu, Q.; Lu, H.; Shi, Z.; Wu, F.; Guo, J.; Deng, K.; Li, L. 2D ZnIn₂S₄ Nanosheet/1D TiO₂ Nanorod Heterostructure Arrays for Improved Photoelectrochemical Water Splitting. *ACS Appl. Mater. Interfaces* **2014**, *6*, 17200–17207. [CrossRef] [PubMed]
- 76. Ren, X.; Singh, A.K.; Fang, L.; Kanatzidis, M.G.; Tavazza, F.; Davydov, A.V.; Lauhon, L.J. Atom Probe Tomography Analysis of Ag Doping in 2D Layered Material (PbSe)₅ (Bi₂Se₃)₃. *Nano Lett.* **2016**, *16*, 6064–6069. [CrossRef] [PubMed]
- 77. Ji, D.; Wen, Q.; Cao, L.; Kang, Q.; Lin, S.; Zhang, X.; Jiang, L.; Guo, W. Electrokinetically Controlled Asymmetric Ion Transport through 1D/2D Nanofluidic Heterojunctions. *Adv. Mater. Technol.* **2019**, *4*, 1800742. [CrossRef]
- 78. Cho, S.-Y.; Koh, H.-J.; Yoo, H.-W.; Kim, J.-S.; Jung, H.-T. Tunable Volatile-Organic-Compound Sensor by Using Au Nanoparticle Incorporation on MoS₂. *ACS Sens.* **2017**, *2*, 183–189. [CrossRef] [PubMed]
- 79. Cheng, R.; Li, D.; Zhou, H.; Wang, C.; Yin, A.; Jiang, S.; Liu, Y.; Chen, Y.; Huang, Y.; Duan, X. Electroluminescence and Photocurrent Generation from Atomically Sharp WSe₂ /MoS₂ Heterojunction *p–n* Diodes. *Nano Lett.* **2014**, *14*, 5590–5597. [CrossRef]
- 80. Choi, M.S.; Qu, D.; Lee, D.; Liu, X.; Watanabe, K.; Taniguchi, T.; Yoo, W.J. Lateral MoS₂ p–n Junction Formed by Chemical Doping for Use in High-Performance Optoelectronics. *ACS Nano* **2014**, *8*, 9332–9340. [CrossRef]
- 81. Yu, X.; Zhang, S.; Zeng, H.; Wang, Q.J. Lateral Black Phosphorene P–N Junctions Formed via Chemical Doping for High Performance near-Infrared Photodetector. *Nano Energy* **2016**, 25, 34–41. [CrossRef]
- 82. Li, M.-Y.; Shi, Y.; Cheng, C.-C.; Lu, L.-S.; Lin, Y.-C.; Tang, H.-L.; Tsai, M.-L.; Chu, C.-W.; Wei, K.-H.; He, J.-H.; et al. Epitaxial Growth of a Monolayer WSe₂-MoS₂ Lateral p-n Junction with an Atomically Sharp Interface. *Science* **2015**, 349, 524–528. [CrossRef]
- 83. Wu, F.; Zhu, Z.-Q.; Tian, H.; Xing, C.-Y.; Ren, T.; Yan, Z.; Liu, Y.; Xu, Y. Vertical WSe₂/BP/MoS₂ Heterostructures with Tunneling Behaviors and Photodetection. *Appl. Phys. Lett.* **2022**, *121*, 113508. [CrossRef]
- 84. Furchi, M.M.; Pospischil, A.; Libisch, F.; Burgdörfer, J.; Mueller, T. Photovoltaic Effect in an Electrically Tunable van Der Waals Heterojunction. *Nano Lett.* **2014**, *14*, 4785–4791. [CrossRef] [PubMed]
- 85. Buscema, M.; Steele, G.A.; Van Der Zant, H.S.J.; Castellanos-Gomez, A. The Effect of the Substrate on the Raman and Photoluminescence Emission of Single-Layer MoS₂. *Nano Res.* **2014**, *7*, 561–571. [CrossRef]
- Hong, T.; Chamlagain, B.; Wang, T.; Chuang, H.-J.; Zhou, Z.; Xu, Y.-Q. Anisotropic Photocurrent Response at Black Phosphorus– MoS₂ p–n Heterojunctions. Nanoscale 2015, 7, 18537–18541. [CrossRef]
- 87. Pezeshki, A.; Shokouh, S.H.H.; Nazari, T.; Oh, K.; Im, S. Electric and Photovoltaic Behavior of a Few-Layer α-MoTe₂ /MoS₂ Dichalcogenide Heterojunction. *Adv. Mater.* **2016**, *28*, 3216–3222. [CrossRef]
- 88. Zhong, J.; Wu, B.; Madoune, Y.; Wang, Y.; Liu, Z.; Liu, Y. PdSe₂/MoSe₂ Vertical Heterojunction for Self-Powered Photodetector with High Performance. *Nano Res.* **2022**, *15*, 2489–2496. [CrossRef]
- 89. Li, H.-M.; Lee, D.; Qu, D.; Liu, X.; Ryu, J.; Seabaugh, A.; Yoo, W.J. Ultimate Thin Vertical p–n Junction Composed of Two-Dimensional Layered Molybdenum Disulfide. *Nat. Commun.* **2015**, *6*, 6564. [CrossRef] [PubMed]
- 90. Xie, C.; Zeng, L.; Zhang, Z.; Tsang, Y.-H.; Luo, L.; Lee, J.-H. High-Performance Broadband Heterojunction Photodetectors Based on Multilayered PtSe₂ Directly Grown on a Si Substrate. *Nanoscale* **2018**, *10*, 15285–15293.
- 91. Lin, S.; Li, X.; Zhang, S.; Wang, P.; Xu, Z.; Zhong, H.; Wu, Z.; Chen, H. Graphene/CdTe Heterostructure Solar Cell and Its Enhancement with Photo-Induced Doping. *Appl. Phys. Lett.* **2015**, *107*, 191106. [CrossRef]
- 92. Wang, Y.; Zhang, Y.; Lu, Y.; Xu, W.; Mu, H.; Chen, C.; Qiao, H.; Song, J.; Li, S.; Sun, B.; et al. Hybrid Graphene–Perovskite Phototransistors with Ultrahigh Responsivity and Gain. *Adv. Opt. Mater.* **2015**, *3*, 1389–1396.
- 93. Ye, Y.; Dai, Y.; Dai, L.; Shi, Z.; Liu, N.; Wang, F.; Fu, L.; Peng, R.; Wen, X.; Chen, Z.; et al. High-Performance Single CdS Nanowire (Nanobelt) Schottky Junction Solar Cells with Au/Graphene Schottky Electrodes. *ACS Appl. Mater. Interfaces* **2010**, *2*, 3406–3410. [PubMed]
- 94. Zhang, L.; Fan, L.; Li, Z.; Shi, E.; Li, X.; Li, H.; Ji, C.; Jia, Y.; Wei, J.; Wang, K.; et al. Graphene-CdSe Nanobelt Solar Cells with Tunable Configurations. *Nano Res.* **2011**, *4*, 891–900. [CrossRef]
- 95. Gan, X.; Shiue, R.-J.; Gao, Y.; Meric, I.; Heinz, T.F.; Shepard, K.; Hone, J.; Assefa, S.; Englund, D. Chip-Integrated Ultrafast Graphene Photodetector with High Responsivity. *Nat. Photon.* **2013**, *7*, 883–887. [CrossRef]
- 96. Furchi, M.; Urich, A.; Pospischil, A.; Lilley, G.; Unterrainer, K.; Detz, H.; Klang, P.; Andrews, A.M.; Schrenk, W.; Strasser, G.; et al. Microcavity-Integrated Graphene Photodetector. *Nano Lett.* **2012**, 12, 2773–2777. [CrossRef] [PubMed]
- 97. Tang, L.; Kocabas, S.E.; Latif, S.; Okyay, A.K.; Ly-Gagnon, D.-S.; Saraswat, K.C.; Miller, D.A.B. Nanometre-Scale Germanium Photodetector Enhanced by a near-Infrared Dipole Antenna. *Nat. Photon.* **2008**, *2*, 226–229. [CrossRef]
- 98. Qasim, M.; Sulaman, M.; Bukhtiar, A.; Deng, B.; Jalal, A.; Sandali, Y.; Shah, N.H.; Li, C.; Dastgeer, G.; Bin, H. High-Performance Self-Powered Broadband Schottky Junction Photodetector Based on Graphene-Silicon van Der Waals Heterostructure. *Energy Technol.* 2023, 11, 2300492. [CrossRef]
- 99. Eastman, D.E. Photoelectric Work Functions of Transition, Rare-Earth, and Noble Metals. Phys. Rev. B 1970, 2, 1–2. [CrossRef]
- 100. Lince, J.R.; Carré, D.J.; Fleischauer, P.D. Schottky-Barrier Formation on a Covalent Semiconductor without Fermi-Level Pinning: The Metal- MoS₂ (0001) Interface. *Phys. Rev. B* **1987**, *36*, 1647–1656. [CrossRef] [PubMed]
- 101. Fontana, M.; Deppe, T.; Boyd, A.K.; Rinzan, M.; Liu, A.Y.; Paranjape, M.; Barbara, P. Electron-Hole Transport and Photovoltaic Effect in Gated MoS₂ Schottky Junctions. *Sci. Rep.* **2013**, *3*, 1634.

Processes **2024**, 12, 1728 25 of 27

102. Dai, M.; Chen, H.; Feng, R.; Feng, W.; Hu, Y.; Yang, H.; Liu, G.; Chen, X.; Zhang, J.; Xu, C.-Y.; et al. A Dual-Band Multilayer InSe Self-Powered Photodetector with High Performance Induced by Surface Plasmon Resonance and Asymmetric Schottky Junction. *ACS Nano* 2018, 12, 8739–8747. [CrossRef]

- 103. Gong, F.; Fang, H.; Wang, P.; Su, M.; Li, Q.; Ho, J.C.; Chen, X.; Lu, W.; Liao, L.; Wang, J.; et al. Visible to Near-Infrared Photodetectors Based on MoS₂ Vertical Schottky Junctions. *Nanotechnology* **2017**, *28*, 484002. [CrossRef] [PubMed]
- 104. Luo, M.; Wu, F.; Long, M.; Chen, X. WSe₂ /Au Vertical Schottky Junction Photodetector with Low Dark Current and Fast Photoresponse. *Nanotechnology* **2018**, 29, 444001. [CrossRef]
- 105. Periyanagounder, D.; Gnanasekar, P.; Varadhan, P.; He, J.-H.; Kulandaivel, J. High Performance, Self-Powered Photodetectors Based on a Graphene/Silicon Schottky Junction Diode. *J. Mater. Chem. C* **2018**, *6*, 9545–9551. [CrossRef]
- 106. Luo, Y.; Yan, X.; Zhang, J.; Li, B.; Wu, Y.; Lu, Q.; Jin, C.; Zhang, X.; Ren, X. A Graphene/Single GaAs Nanowire Schottky Junction Photovoltaic Device. *Nanoscale* **2018**, *10*, 9212–9217. [CrossRef]
- 107. Xiang, D.; Han, C.; Hu, Z.; Lei, B.; Liu, Y.; Wang, L.; Hu, W.P.; Chen, W. Surface Transfer Doping-Induced, High-Performance Graphene/Silicon Schottky Junction-Based, Self-Powered Photodetector. *Small* **2015**, 37, 4829–4836. [CrossRef] [PubMed]
- 108. Yu, T.; Wang, F.; Xu, Y.; Ma, L.; Pi, X.; Yang, D. Graphene Coupled with Silicon Quantum Dots for High-Performance Bulk-Silicon-Based Schottky-Junction Photodetectors. *Adv. Mater.* **2016**, *28*, 4912–4919.
- 109. Wu, J.; Yang, Z.; Qiu, C.; Zhang, Y.; Wu, Z.; Yang, J.; Lu, Y.; Li, J.; Yang, D.; Hao, R.; et al. Enhanced Performance of a Graphene/GaAs Self-Driven near-Infrared Photodetector with Upconversion Nanoparticles. *Nanoscale* **2018**, *10*, 8023–8030. [CrossRef]
- 110. Li, H.; Bowen, C.R.; Yang, Y. Scavenging Energy Sources Using Ferroelectric Materials. *Adv. Funct. Mater.* **2021**, *31*, 2100905. [CrossRef]
- 111. Paillard, C.; Bai, X.; Infante, I.C.; Guennou, M.; Geneste, G.; Alexe, M.; Kreisel, J.; Dkhil, B. Photovoltaics with Ferroelectrics: Current Status and Beyond. *Adv. Mater.* **2016**, *28*, 5153–5168.
- 112. Han, X.; Ji, Y.; Yang, Y. Ferroelectric Photovoltaic Materials and Devices. Adv. Funct. Mater. 2022, 32, 2109625. [CrossRef]
- 113. Nayak, P.K.; Mahesh, S.; Snaith, H.J.; Cahen, D. Photovoltaic Solar Cell Technologies: Analysing the State of the Art. *Nat. Rev. Mater.* **2019**, *4*, 269–285. [CrossRef]
- 114. Yang, S.Y.; Seidel, J.; Byrnes, S.J.; Shafer, P.; Yang, C.-H.; Rossell, M.D.; Yu, P.; Chu, Y.-H.; Scott, J.F.; Ager, J.W.; et al. Above-Bandgap Voltages from Ferroelectric Photovoltaic Devices. *Nat. Nanotechnol.* **2010**, *5*, 143–147. [CrossRef] [PubMed]
- 115. Hatada, H.; Nakamura, M.; Sotome, M.; Kaneko, Y.; Ogawa, N.; Morimoto, T.; Tokura, Y.; Kawasaki, M. Defect Tolerant Zero-Bias Topological Photocurrent in a Ferroelectric Semiconductor. *Proc. Natl. Acad. Sci. USA* **2020**, *117*, 20411–20415. [CrossRef] [PubMed]
- 116. Zhang, Y.J.; Ideue, T.; Onga, M.; Qin, F.; Suzuki, R.; Zak, A.; Tenne, R.; Smet, J.H.; Iwasa, Y. Enhanced Intrinsic Photovoltaic Effect in Tungsten Disulfide Nanotubes. *Nature* **2019**, *570*, 349–353. [CrossRef] [PubMed]
- 117. Li, Y.; Fu, J.; Mao, X.; Chen, C.; Liu, H.; Gong, M.; Zeng, H. Enhanced Bulk Photovoltaic Effect in Two-Dimensional Ferroelectric CuInP₂S₆. *Nat. Commun.* **2021**, 12, 5896. [CrossRef] [PubMed]
- 118. Yang, D.; Wu, J.; Zhou, B.T.; Liang, J.; Ideue, T.; Siu, T.; Awan, K.M.; Watanabe, K.; Taniguchi, T.; Iwasa, Y.; et al. Spontaneous-Polarization-Induced Photovoltaic Effect in Rhombohedrally Stacked MoS₂. *Nat. Photon.* **2022**, *16*, 469–474. [CrossRef]
- 119. Zhang, Y.; Holder, T.; Ishizuka, H.; De Juan, F.; Nagaosa, N.; Felser, C.; Yan, B. Switchable Magnetic Bulk Photovoltaic Effect in the Two-Dimensional Magnet CrI₃. *Nat. Commun.* **2019**, *10*, 3783. [CrossRef]
- 120. Song, T.; Cai, X.; Tu, M.W.-Y.; Zhang, X.; Huang, B.; Wilson, N.P.; Seyler, K.L.; Zhu, L.; Taniguchi, T.; Watanabe, K.; et al. Giant Tunneling Magnetoresistance in Spin-Filter van Der Waals Heterostructures. *Science* 2018, 360, 1214–1218. [CrossRef] [PubMed]
- 121. Yang, M.-M.; Kim, D.J.; Alexe, M. Flexo-Photovoltaic Effect. Science 2018, 360, 904–907. [CrossRef]
- 122. Qiu, Q.; Huang, Z. Photodetectors of 2D Materials from Ultraviolet to Terahertz Waves. Adv. Mater. 2021, 33, 2008126. [CrossRef]
- 123. Tielrooij, K.J.; Piatkowski, L.; Massicotte, M.; Woessner, A.; Ma, Q.; Lee, Y.; Myhro, K.S.; Lau, C.N.; Jarillo-Herrero, P.; Van Hulst, N.F.; et al. Generation of Photovoltage in Graphene on a Femtosecond Timescale through Efficient Carrier Heating. *Nat. Nanotechnol.* **2015**, *10*, 437–443. [CrossRef]
- 124. Gabor, N.M.; Song, J.C.W.; Ma, Q.; Nair, N.L.; Taychatanapat, T.; Watanabe, K.; Taniguchi, T.; Levitov, L.S.; Jarillo-Herrero, P. Hot Carrier–Assisted Intrinsic Photoresponse in Graphene. *Science* **2011**, *334*, 648–652. [CrossRef]
- 125. Wei, P.; Bao, W.; Pu, Y.; Lau, C.N.; Shi, J. Anomalous Thermoelectric Transport of Dirac Particles in Graphene. *Phys. Rev. Lett.* **2009**, *102*, 166808. [CrossRef] [PubMed]
- 126. Cai, W.; Moore, A.L.; Zhu, Y.; Li, X.; Chen, S.; Shi, L.; Ruoff, R.S. Thermal Transport in Suspended and Supported Monolayer Graphene Grown by Chemical Vapor Deposition. *Nano Lett.* **2010**, *10*, 1645–1651. [CrossRef]
- 127. Basko, D.M.; Aleiner, I.L. Interplay of Coulomb and Electron-Phonon Interactions in Graphene. *Phys. Rev. B* **2008**, 77, 041409. [CrossRef]
- 128. Xu, X.; Gabor, N.M.; Alden, J.S.; Van Der Zande, A.M.; McEuen, P.L. Photo-Thermoelectric Effect at a Graphene Interface Junction. *Nano Lett.* **2010**, *10*, 562–566. [CrossRef] [PubMed]
- 129. Mak, K.F.; Lee, C.; Hone, J.; Shan, J.; Heinz, T.F. Atomically Thin MoS₂: A New Direct-Gap Semiconductor. *Phys. Rev. Lett.* **2010**, 105, 136805. [CrossRef]
- 130. Wu, J.; Schmidt, H.; Amara, K.K.; Xu, X.; Eda, G.; Özyilmaz, B. Large Thermoelectricity via Variable Range Hopping in Chemical Vapor Deposition Grown Single-Layer MoS₂. *Nano Lett.* **2014**, *14*, 2730–2734. [CrossRef] [PubMed]

Processes 2024, 12, 1728 26 of 27

131. Wi, S.; Kim, H.; Chen, M.; Nam, H.; Guo, L.J.; Meyhofer, E.; Liang, X. Enhancement of Photovoltaic Response in Multilayer MoS ₂ Induced by Plasma Doping. *ACS Nano* **2014**, *8*, 5270–5281. [CrossRef]

- 132. Zhang, Y.; Li, H.; Wang, L.; Wang, H.; Xie, X.; Zhang, S.-L.; Liu, R.; Qiu, Z.-J. Photothermoelectric and Photovoltaic Effects Both Present in MoS₂. *Sci. Rep.* **2015**, *5*, 7938. [CrossRef] [PubMed]
- 133. Buscema, M.; Barkelid, M.; Zwiller, V.; Van Der Zant, H.S.J.; Steele, G.A.; Castellanos-Gomez, A. Large and Tunable Photothermoelectric Effect in Single-Layer MoS₂. *Nano Lett.* **2013**, *13*, 358–363. [CrossRef]
- 134. Das, S.; Appenzeller, J. WSe₂ Field Effect Transistors with Enhanced Ambipolar Characteristics. *Appl. Phys. Lett.* **2013**, *103*, 103501. [CrossRef]
- 135. Groenendijk, D.J.; Buscema, M.; Steele, G.A.; Michaelis De Vasconcellos, S.; Bratschitsch, R.; Van Der Zant, H.S.J.; Castellanos-Gomez, A. Photovoltaic and Photothermoelectric Effect in a Double-Gated WSe₂ Device. *Nano Lett.* **2014**, *14*, 5846–5852. [CrossRef]
- 136. Low, T.; Engel, M.; Steiner, M.; Avouris, P. Origin of Photoresponse in Black Phosphorus Phototransistors. *Phys. Rev. B* **2014**, 90, 081408. [CrossRef]
- 137. Engel, M.; Steiner, M.; Avouris, P. Black Phosphorus Photodetector for Multispectral, High-Resolution Imaging. *Nano Lett.* **2014**, 14, 6414–6417. [CrossRef]
- 138. Lai, J.; Liu, Y.; Ma, J.; Zhuo, X.; Peng, Y.; Lu, W.; Liu, Z.; Chen, J.; Sun, D. Broadband Anisotropic Photoresponse of the "Hydrogen Atom" Version Type-II Weyl Semimetal Candidate TaIrTe₄. *ACS Nano* **2018**, 12, 4055–4061. [CrossRef] [PubMed]
- 139. Li, G.; Zhang, H.; Li, Y.; Yin, S.; Kan, X.; Wei, W.; Du, H.; Ge, B.; An, C.; Tian, M.; et al. Ultra-Broadband, Fast, and Polarization-Sensitive Photoresponse of Low-Symmetry 2D NdSb₂. *Nano Res.* **2022**, *15*, 5469–5475. [CrossRef]
- 140. Li, G.; Yin, S.; Tan, C.; Chen, L.; Yu, M.; Li, L.; Yan, F. Fast Photothermoelectric Response in CVD-Grown PdSe₂ Photodetectors with In-Plane Anisotropy. *Adv. Funct. Mater.* **2021**, *31*, 2104787. [CrossRef]
- 141. Yang, S.; Wang, C.; Ataca, C.; Li, Y.; Chen, H.; Cai, H.; Suslu, A.; Grossman, J.C.; Jiang, C.; Liu, Q.; et al. Self-Driven Photodetector and Ambipolar Transistor in Atomically Thin GaTe-MoS₂ p–n vdW Heterostructure. *ACS Appl. Mater. Interfaces* **2016**, *8*, 2533–2539. [CrossRef]
- 142. Yu, X.; Shen, Y.; Liu, T.; Wu, T.; Jie Wang, Q. Photocurrent Generation in Lateral Graphene P-n Junction Created by Electron-Beam Irradiation. *Sci. Rep.* **2015**, *5*, 12014. [CrossRef] [PubMed]
- 143. Wu, W.; Zhang, Q.; Zhou, X.; Li, L.; Su, J.; Wang, F.; Zhai, T. Self-Powered Photovoltaic Photodetector Established on Lateral Monolayer MoS2-WS2 Heterostructures. *Nano Energy* **2018**, *51*, 45–53. [CrossRef]
- 144. Liu, X.; Yang, X.; Gao, G.; Yang, Z.; Liu, H.; Li, Q.; Lou, Z.; Shen, G.; Liao, L.; Pan, C.; et al. Enhancing Photoresponsivity of Self-Aligned MoS ₂ Field-Effect Transistors by Piezo-Phototronic Effect from GaN Nanowires. *ACS Nano* **2016**, *10*, 7451–7457. [CrossRef]
- 145. Li, G.; Liu, L.; Wu, G.; Chen, W.; Qin, S.; Wang, Y.; Zhang, T. Self-Powered UV–Near Infrared Photodetector Based on Reduced Graphene Oxide/n-Si Vertical Heterojunction. *Small* **2016**, *12*, 5019–5026. [CrossRef] [PubMed]
- 146. Aldalbahi, A.; Rivera, M.; Rahaman, M.; Zhou, A.; Mohammed Alzuraiqi, W.; Feng, P. High-Performance and Self-Powered Deep UV Photodetectors Based on High Quality 2D Boron Nitride Nanosheets. *Nanomaterials* **2017**, 7, 454. [CrossRef] [PubMed]
- 147. Duan, L.; He, F.; Tian, Y.; Sun, B.; Fan, J.; Yu, X.; Ni, L.; Zhang, Y.; Chen, Y.; Zhang, W. Fabrication of Self-Powered Fast-Response Ultraviolet Photodetectors Based on Graphene/ZnO:Al Nanorod-Array-Film Structure with Stable Schottky Barrier. *ACS Appl. Mater. Interfaces* 2017, 9, 8161–8168. [CrossRef] [PubMed]
- 148. Zeng, L.-H.; Wang, M.-Z.; Hu, H.; Nie, B.; Yu, Y.-Q.; Wu, C.-Y.; Wang, L.; Hu, J.-G.; Xie, C.; Liang, F.-X.; et al. Monolayer Graphene/Germanium Schottky Junction As High-Performance Self-Driven Infrared Light Photodetector. *ACS Appl. Mater. Interfaces* 2013, 5, 9362–9366. [CrossRef] [PubMed]
- 149. Lv, P.; Zhang, X.; Zhang, X.; Deng, W.; Jie, J. High-Sensitivity and Fast-Response Graphene/Crystalline Silicon Schottky Junction-Based Near-IR Photodetectors. *IEEE Electron Device Lett.* **2013**, 34, 1337–1339. [CrossRef]
- 150. Li, L.; Liu, X.; Li, Y.; Xu, Z.; Wu, Z.; Han, S.; Tao, K.; Hong, M.; Luo, J.; Sun, Z. Two-Dimensional Hybrid Perovskite-Type Ferroelectric for Highly Polarization-Sensitive Shortwave Photodetection. *J. Am. Chem. Soc.* **2019**, *141*, 2623–2629. [CrossRef] [PubMed]
- 151. Aftab, S.; Shehzad, M.A.; Salman Ajmal, H.M.; Kabir, F.; Iqbal, M.Z.; Al-Kahtani, A.A. Bulk Photovoltaic Effect in Two-Dimensional Distorted MoTe₂. *ACS Nano* **2023**, *17*, 17884–17896. [CrossRef]
- 152. Peng, Y.; Liu, X.; Sun, Z.; Ji, C.; Li, L.; Wu, Z.; Wang, S.; Yao, Y.; Hong, M.; Luo, J. Exploiting the Bulk Photovoltaic Effect in a 2D Trilayered Hybrid Ferroelectric for Highly Sensitive Polarized Light Detection. *Angew. Chem. Int. Ed.* **2020**, *59*, 3933–3937. [CrossRef]
- 153. Li, D.; Qin, J.-K.; Zhu, B.; Yue, L.-Q.; Huang, P.-Y.; Zhu, C.; Zhou, F.; Zhen, L.; Xu, C.-Y. Intercorrelated Ferroelectricity and Bulk Photovoltaic Effect in Two-Dimensional Sn₂P₂S₆ Semiconductor for Polarization-Sensitive Photodetection. *ACS Nano* **2024**, *18*, 9636–9644. [CrossRef] [PubMed]
- 154. Cai, X.; Sushkov, A.B.; Suess, R.J.; Jadidi, M.M.; Jenkins, G.S.; Nyakiti, L.O.; Myers-Ward, R.L.; Li, S.; Yan, J.; Gaskill, D.K.; et al. Sensitive Room-Temperature Terahertz Detection via the Photothermoelectric Effect in Graphene. *Nat. Nanotechnol.* **2014**, *9*, 814–819. [CrossRef] [PubMed]
- 155. Hsu, A.L.; Herring, P.K.; Gabor, N.M.; Ha, S.; Shin, Y.C.; Song, Y.; Chin, M.; Dubey, M.; Chandrakasan, A.P.; Kong, J.; et al. Graphene-Based Thermopile for Thermal Imaging Applications. *Nano Lett.* **2015**, *15*, 7211–7216. [CrossRef] [PubMed]

Processes **2024**, 12, 1728 27 of 27

156. Badioli, M.; Woessner, A.; Tielrooij, K.J.; Nanot, S.; Navickaite, G.; Stauber, T.; García De Abajo, F.J.; Koppens, F.H.L. Phonon-Mediated Mid-Infrared Photoresponse of Graphene. *Nano Lett.* **2014**, *14*, 6374–6381. [CrossRef] [PubMed]

- 157. Tong, J.; Muthee, M.; Chen, S.-Y.; Yngvesson, S.K.; Yan, J. Antenna Enhanced Graphene THz Emitter and Detector. *Nano Lett.* **2015**, *15*, 5295–5301. [CrossRef] [PubMed]
- 158. Viti, L.; Hu, J.; Coquillat, D.; Knap, W.; Tredicucci, A.; Politano, A.; Vitiello, M.S. Black Phosphorus Terahertz Photodetectors. *Adv. Mater.* 2015, 27, 5567–5572. [CrossRef] [PubMed]
- 159. He, X.; Wang, X.; Nanot, S.; Cong, K.; Jiang, Q.; Kane, A.A.; Goldsmith, J.E.M.; Hauge, R.H.; Léonard, F.; Kono, J. Photothermoelectric p–n Junction Photodetector with Intrinsic Broadband Polarimetry Based on Macroscopic Carbon Nanotube Films. *ACS Nano* 2013, 7, 7271–7277. [CrossRef] [PubMed]
- 160. He, X.; Fujimura, N.; Lloyd, J.M.; Erickson, K.J.; Talin, A.A.; Zhang, Q.; Gao, W.; Jiang, Q.; Kawano, Y.; Hauge, R.H.; et al. Carbon Nanotube Terahertz Detector. *Nano Lett.* **2014**, *14*, 3953–3958. [CrossRef] [PubMed]
- 161. Léonard, F.; Song, E.; Li, Q.; Swartzentruber, B.; Martinez, J.A.; Wang, G.T. Simultaneous Thermoelectric and Optoelectronic Characterization of Individual Nanowires. *Nano Lett.* **2015**, *15*, 8129–8135. [CrossRef]
- 162. Lai, Y.; Tsai, C.; Chang, C.; Huang, C.; Hsiao, V.K.S.; Su, Y.O. Photothermoelectric Effects in Nanoporous Silicon. *Adv. Mater.* **2016**, 28, 2644–2648. [CrossRef]
- 163. Yi, S.-G.; Kim, S.H.; Park, S.; Oh, D.; Choi, H.Y.; Lee, N.; Choi, Y.J.; Yoo, K.-H. Mo_{1-x}W_xSe₂-Based Schottky Junction Photovoltaic Cells. *ACS Appl. Mater. Interfaces* **2016**, *8*, 33811–33820. [CrossRef] [PubMed]
- 164. Baugher, B.W.H.; Churchill, H.O.H.; Yang, Y.; Jarillo-Herrero, P. Optoelectronic Devices Based on Electrically Tunable p–n Diodes in a Monolayer Dichalcogenide. *Nat. Nanotechnol.* **2014**, *9*, 262–267. [CrossRef] [PubMed]
- 165. Buscema, M.; Groenendijk, D.J.; Steele, G.A.; Van Der Zant, H.S.J.; Castellanos-Gomez, A. Photovoltaic Effect in Few-Layer Black Phosphorus PN Junctions Defined by Local Electrostatic Gating. *Nat. Commun.* **2014**, *5*, 4651. [CrossRef]
- 166. Memaran, S.; Pradhan, N.R.; Lu, Z.; Rhodes, D.; Ludwig, J.; Zhou, Q.; Ogunsolu, O.; Ajayan, P.M.; Smirnov, D.; Fernández-Domínguez, A.I.; et al. Pronounced Photovoltaic Response from Multilayered Transition-Metal Dichalcogenides PN-Junctions. *Nano Lett.* **2015**, *15*, 7532–7538. [CrossRef] [PubMed]
- 167. Tsai, M.-L.; Su, S.-H.; Chang, J.-K.; Tsai, D.-S.; Chen, C.-H.; Wu, C.-I.; Li, L.-J.; Chen, L.-J.; He, J.-H. Monolayer MoS₂ Heterojunction Solar Cells. *ACS Nano* **2014**, *8*, 8317–8322. [CrossRef] [PubMed]
- 168. Lin, S.; Li, X.; Wang, P.; Xu, Z.; Zhang, S.; Zhong, H.; Wu, Z.; Xu, W.; Chen, H. Interface Designed MoS₂/GaAs Heterostructure Solar Cell with Sandwich Stacked Hexagonal Boron Nitride. *Sci. Rep.* **2015**, *5*, 15103. [CrossRef] [PubMed]
- 169. Lin, S.; Wang, P.; Li, X.; Wu, Z.; Xu, Z.; Zhang, S.; Xu, W. Gate Tunable Monolayer MoS₂/InP Heterostructure Solar Cells. *Appl. Phys. Lett.* **2015**, *107*, 153904. [CrossRef]
- 170. Yu, W.J.; Liu, Y.; Zhou, H.; Yin, A.; Li, Z.; Huang, Y.; Duan, X. Highly Efficient Gate-Tunable Photocurrent Generation in Vertical Heterostructures of Layered Materials. *Nat. Nanotechnol.* **2013**, *8*, 952–958. [CrossRef] [PubMed]
- 171. Chen, Z.; Liu, H.; Chen, X.; Chu, G.; Chu, S.; Zhang, H. Wafer-Size and Single-Crystal MoSe₂ Atomically Thin Films Grown on GaN Substrate for Light Emission and Harvesting. *ACS Appl. Mater. Interfaces* **2016**, *8*, 20267–20273. [CrossRef]
- 172. Wang, P.; Lin, S.; Ding, G.; Li, X.; Wu, Z.; Zhang, S.; Xu, Z.; Xu, S.; Lu, Y.; Xu, W.; et al. Enhanced Monolayer MoS₂/InP Heterostructure Solar Cells by Graphene Quantum Dots. *Appl. Phys. Lett.* **2016**, *108*, 163901. [CrossRef]
- 173. Lin, S.; Wu, Z.; Li, X.; Zhang, Y.; Zhang, S.; Wang, P.; Panneerselvam, R.; Li, J. Stable 16.2% Efficient Surface Plasmon-Enhanced Graphene/GaAs Heterostructure Solar Cell. *Adv. Energy Mater.* **2016**, *6*, 1600822. [CrossRef]
- 174. Hao, L.Z.; Gao, W.; Liu, Y.J.; Han, Z.D.; Xue, Q.Z.; Guo, W.Y.; Zhu, J.; Li, Y.R. High-Performance n-MoS₂/i-SiO₂/p-Si Heterojunction Solar Cells. *Nanoscale* **2015**, *7*, 8304–8308. [CrossRef]
- 175. Gehring, P.; Urcuyo, R.; Duong, D.L.; Burghard, M.; Kern, K. Thin-Layer Black Phosphorus/GaAs Heterojunction p-n Diodes. *Appl. Phys. Lett.* **2015**, *106*, 233110. [CrossRef]
- 176. Ji, W.; Yao, K.; Liang, Y.C. Bulk Photovoltaic Effect at Visible Wavelength in Epitaxial Ferroelectric BiFeO₃ Thin Films. *Adv. Mater.* **2010**, 22, 1763–1766. [CrossRef] [PubMed]
- 177. Zenkevich, A.; Matveyev, Y.; Maksimova, K.; Gaynutdinov, R.; Tolstikhina, A.; Fridkin, V. Giant Bulk Photovoltaic Effect in Thin Ferroelectric BaTiO₃ Films. *Phys. Rev. B* **2014**, *90*, 161409. [CrossRef]
- 178. Grinberg, I.; West, D.V.; Torres, M.; Gou, G.; Stein, D.M.; Wu, L.; Chen, G.; Gallo, E.M.; Akbashev, A.R.; Davies, P.K.; et al. Perovskite Oxides for Visible-Light-Absorbing Ferroelectric and Photovoltaic Materials. *Nature* **2013**, *503*, 509–512. [CrossRef] [PubMed]
- 179. Pal, S.; Swain, A.B.; Biswas, P.P.; Murali, D.; Pal, A.; Nanda, B.R.K.; Murugavel, P. Giant Photovoltaic Response in Band Engineered Ferroelectric Perovskite. *Sci. Rep.* **2018**, *8*, 8005. [CrossRef]
- 180. Peng, L.; Xie, W. Theoretical and Experimental Investigations on the Bulk Photovoltaic Effect in Lead-Free Perovskites MASnI₃ and FASnI₃. *RSC Adv.* **2020**, *10*, 14679–14688. [CrossRef]

Disclaimer/Publisher's Note: The statements, opinions and data contained in all publications are solely those of the individual author(s) and contributor(s) and not of MDPI and/or the editor(s). MDPI and/or the editor(s) disclaim responsibility for any injury to people or property resulting from any ideas, methods, instructions or products referred to in the content.